Physics – Uspekhi **48** (5) 487 – 514 (2005)

INSTRUMENTS AND METHODS OF INVESTIGATION PACS numbers: **52.77.–j**, **81.15.–z**, **81.65.–b**, 82.45.Bb

Modification of material properties and coating deposition using plasma jets

A D Pogrebnjak, Yu N Tyurin

DOI: 10.1070/PU2005v048n05ABEH002055

Contents

Abstract. The review is concerned with the current status of research on the use of plasma jets for the modification of surface properties of metalware, as well as of investigations of doping and mass transfer of elements. The effect of thermal plasma parameters on the efficiency of surface processing of metal materials is discussed. The structure and properties of protective coatings produced by exposure to pulsed plasmas are analyzed. A new direction for the production of combined coatings is considered. Their structure and properties were studied by the example of Fe, Cu, steels, and alloys, including titanium alloys; the modification process was shown to be controllable by the action of pulsed plasma jets. The physical factors that affect the modification process and the coating deposition, and their effect on the structure and properties of metallic, ceramic–metal, and ceramic coatings were analyzed.

A D Pogrebnjak Sumy Institute for Surface Modification, P.O.Box 163, ul. Romenskaya 87, Bldg. "M", 40030 Sumy, Ukraine
Tel. (10-380-542) 22-03 38
E-mail: apogrebnjak@ua.fm
Yu N Tyurin Paton Institute for Electric Welding, National Academy of Sciences of Ukraine
ul. Bozhenko 11, 30650 Kiev, Ukraine
Tel. (10-380-44) 261-50 34
E-mail: ytyurin@i.com.ua

Received 9 September 2004
Uspekhi Fizicheskikh Nauk **175** (5) 515 – 544 (2005)
Translated by E N Ragozin; edited by A M Semikhatov

1. Introduction

Thermal plasmas in a local thermodynamic equilibrium can be produced by a high-intensity arc discharge (the current $I > 300$ A) or a radio-frequency discharge (RFD) for a high power density and pressures exceeding 10 kPa (0.1 atm). In such plasmas, the electron and heavy-particle temperatures are equal and the density depends only on the temperature (chemical equilibrium). The 1960s saw the beginning of intensive development of thermal plasma technology, and by the 1980s, the main area of its application took shape — materials technology. Since the end of the 20th century, material processing by thermal plasmas has attracted the progressively increasing attention of researchers for the solution of applied problems, including applications in different branches of the industry.

2. Material processing by thermal plasmas

Material processing by thermal plasmas is employed to produce coatings and modify material properties, which is one of the main, most significant physicotechnical problems of material technology. This area embraces not only the development of new materials but also the purification of materials being used, material conservation (by way of hard lining, deposition of coatings, etc.), and development of new processing techniques that are higher in energy efficiency, more productive, and cause less damage to the environment. High-temperature plasma processing now plays an important

part in the advancement of these directions. Its potential for the development of new material-related technologies is universally recognized, and many scientific laboratories throughout the world are already engaged in research in this interesting area.

Powder compaction, plasma deposition of protective coatings, production of composite coatings — these are typical examples where plasma is employed as a high-power thermal source. Worldwide, the cost of work using plasma deposition is estimated at millions of dollars annually. This technology is employed primarily in the aircraft industry, medical prosthetics, mineral processing, and the chemical industry.

Wire-arc deposition is an inexpensive and efficient way of depositing coatings on metals and alloys. It is attracting increasing attention of automakers. Although the method of coating metal and alloy surfaces by way of chemical vapor deposition using high-temperature plasmas is still in its research and development stage, its industrial employment is highly promising, because it allows obtaining high-quality ceramics, diamonds, and superconducting films.

Yet another area that has gained acceptance nowadays and has been very promising is the plasma synthesis of fine powders of different chemical compounds, including metal oxides, carbides, nitrides, borides, and their combination. To date, of practical interest are nanometer-scale particles, which are the key element for obtaining high-performance engineering materials.

2.1 Powder compaction with the aid of thermal plasmas

Powder compaction is one of the simplest and most successfully advancing technologies of material processing. This includes the in-flight melting of a material into macroparticles and its subsequent cooling and freezing, which takes place before it is deposited on the bottom of a compaction chamber or in the corresponding collector, depending on the density of particles and their size. Using either a direct current (dc) or inductively coupled plasma burners [radio-frequency (RF) burners], compaction and spheroidizing are performed on a wide diversity of materials ranging from metals with a low melting point (like copper and nickel) to ceramic oxides (like aluminum oxide and yttrium-stabilized zirconium oxide) and refractory metals (like molybdenum and tungsten). Figure 1 shows typical photographs for aluminum, molybdenum, and tungsten powders (the average particle diameter ranges from 45 to 76 μm). These images, which were obtained with the aid of an electron microscope, reveal the morphology of individual particles prior to and after compaction by inductively coupled RF plasma burners.

2.2 Coating deposition by thermal plasma action

The plasma-assisted deposition of metal, ceramic, and composite material coatings is a well-proven technology, which is now employed to deposit protective coatings and composite materials on an industrial scale. Many applied problems have been solved in aerospace and chemical industries with the use of this technology during the past decade. A typical example is provided by the plasma deposition of yttrium-stabilized zirconium as the heat-protection coating for turbine blades and liners (valves, inner walls) of jet combustion chambers. Antiwear WC-Co or Cr_2O_3 coatings are also finding increasing use in machine building. Another example of the industrial application of plasma deposition is the deposition of titanium alloys and hydroxylapatites on hip joints, furnishing stronger and more durable connections to bone tissue in comparison with those obtained by chemical cementation.

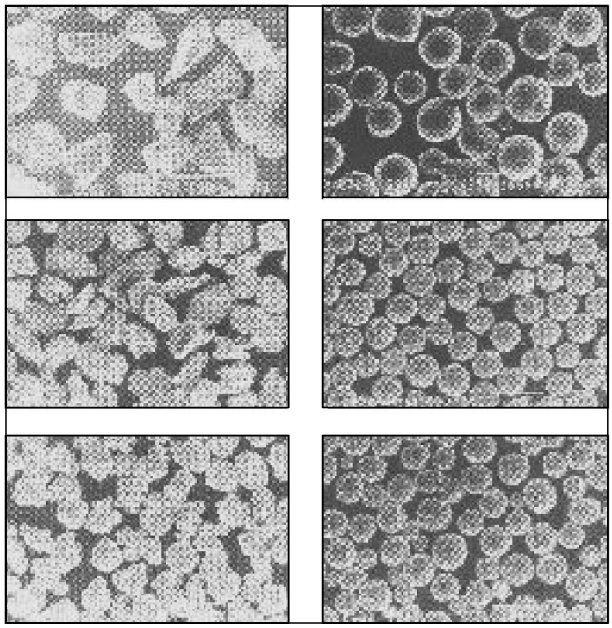

Figure 1. Electron-microscope images of the initial (left) and plasma-compacted (right) aluminum (upper row), molybdenum (middle row), and tungsten (lower row) powders.

In the majority of these approaches, the alternating current of a plasma burner is used as a heat source, such that the powder is melted in its flight, prior to its deposition on the substrate surface. The process is effected in different gaseous media (Ar, Ar/H_2, Ar/He, etc.) at atmospheric or reduced pressure, depending on the chemical composition of the material being deposited. Today, for plasma-deposited coatings and coating deposition, inductively coupled radio-frequency plasma burners are used. Their main advantage consists in the chemical diversity of the plasma gas employed. All this was made possible due to the absence of electrodes, which allows operating in a neutral, oxidizing, or deficient medium (atmosphere) at atmospheric or reduced pressure. It is possible to effect reactive coating deposition, depending on the chemical composition of the plasma gas. In this case, the chemical composition of the resultant coating is different from the initial material. Figure 2 is a schematic representation of the main concepts involving direct current and inductive radio-frequency plasma coupling in coating deposition. This subject has been the concern of several papers [1 – 5].

Wire-arc (WA) deposition is an energy-efficient process, which is the most efficient process in the case of the thermal method of coating deposition. It is widely used in the coating of engineering structures for their corrosion and wear protection [5, 6]. The heat generated by an electric arc initiated between the ends of two wires melts these ends. The molten droplets are carried by the high-speed gas jet and act on a substrate to form the coating (Fig. 3). The wires are continuously fed to ensure a constant gap.

Recent developments in the area of wire-arc deposition have advanced this technology, allowing the production of high-quality coatings [7 – 9]. This technology makes use of air atomization. Its main advantages consist in accessibility and

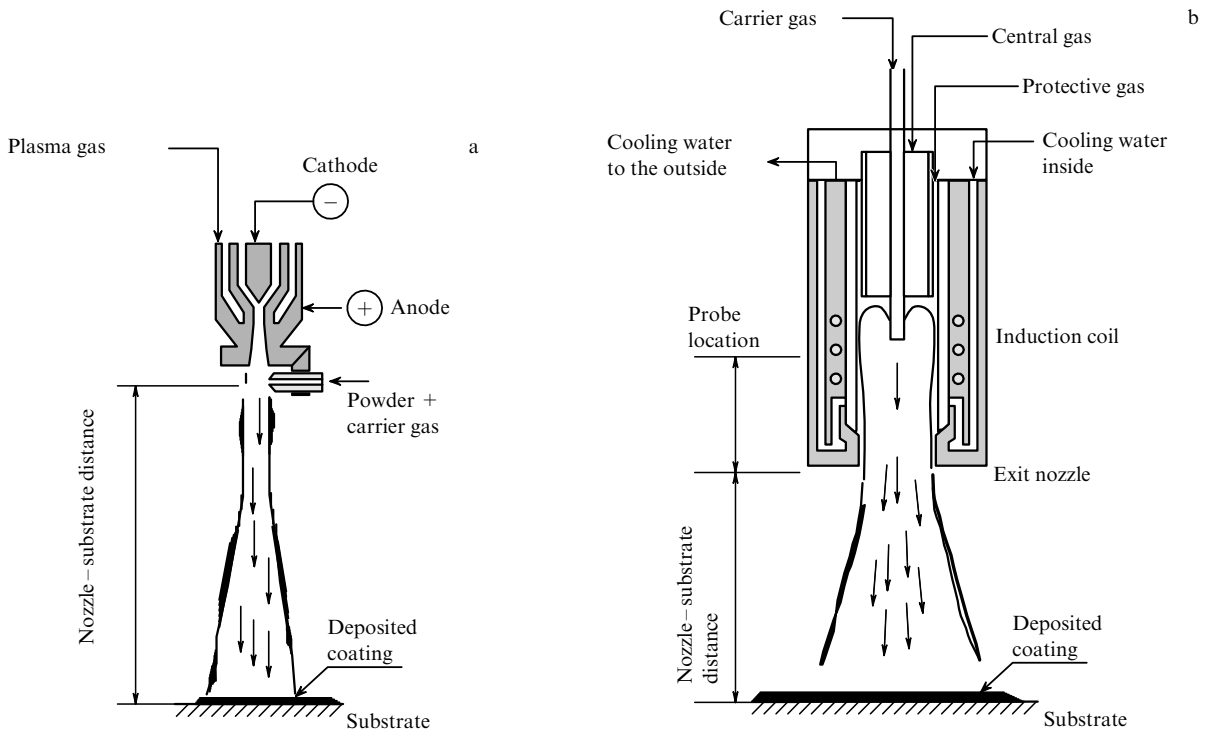

Figure 2. Schematic of plasma injection for a direct current (a) and a radio-frequency mode (b).

saving compressed air. In the course of air atomization in the wire-arc deposition, the content of oxide in the coating being deposited is relatively high owing to the oxidation of molten wire material, which increases the coating hardness to the extent that the abrasive resistance is improved.

However, the oxide content may be a limiting factor as regards high-quality coating production, because the oxides may decrease the coating – substrate adhesion strength. Coatings with a weak adhesion may prematurely exfoliate during operation. In addition, the hard oxide particles that reside in the volume of deposited coatings may present a problem during mechanical processing. Furthermore, the coatings deposited with air atomization quite often exhibit a high porosity, which is a disadvantage, because the corroding liquids have access to the substrate through the coating, thereby reducing its protective capacity. Yet another disadvantage of air atomization is the burning-out of alloying elements (like Cr and C) contained in the initial wires. These elements are significant ingredients for obtaining the requisite coating characteristics. Owing to their burning-out, specific coating characteristics become impossible to obtain. That is why rare gases and CO_2 came into use as the atomizing gas. However, even a CO_2-assisted deposition may result in a strong oxidation of the coating due to penetration of large amounts of air. Moreover, the ingress of large amounts of air can lead to a strong decrease in the temperature and the velocity of the gas flow. To avoid the ingress of air, the atomizing gas flow should be protected from the ambient atmosphere.

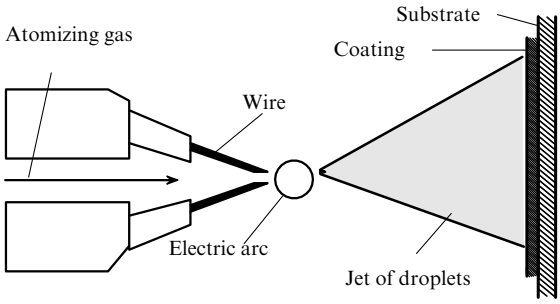

Figure 3. Schematic of a wire-arc plasma jet injection.

Research in the University of Minnesota on wire-arc deposition of stainless steel on aluminum substrates employing CO_2 as the atomizing gas and CO_2 as the protection showed that it is possible to significantly lower the content of oxides for minimum losses of chromium in the coating and a simultaneous lowering of the porosity level [10].

In the course of thermal plasma chemical vapor deposition (TPCVD), a high-energy thermal plasma (with the temperature up to 10^4 K and above) forms precursors of a high-density evaporative phase for the deposition of relatively thick films. Although the TPCVD technology is still in its infancy, it will be used in the cases that are intermediate between slow deposition processes, like plasma-assisted strengthening or physical coating deposition in the form of low-density vapor and CVD, and high-rate high-temperature coating deposition (discussed below in our work).

We consider a typical TPCVD scheme for diamond film deposition. A dc plasma burner generates a high-temperature high-speed plasma jet, which collides with a cooled substrate. At temperatures close to the burner temperatures at the nozzle outlet, which exceed 10^4 K, the initial material injected into the plasma is rapidly vaporized, dissociates, and is accelerated towards the substrate owing to the high velocities (of the order of 1000 m s^{-1}). A boundary layer characterized by steep temperature gradients is formed in front of the cooled substrate. This thin boundary layer and the strong temperature gradients are favorable for the

attainment of the goal pursued. Specific properties of the plasma jet, which collides with the substrate, in combination with a fixed substrate temperature, determine the properties of the boundary layer, including its thickness. Because the boundary layer thickness, like the substrate temperature, affects the gaseous phase and the chemical composition of the surface, these parameters determine the rate of film deposition and its quality.

Owing to intense nonuniform substrate heating by the plasma jet, maintaining the nonuniform temperature is not a simple task. To attain uniformity, the use of different substrate cooling schemes, the organization of the corresponding plasma movement relative to the substrate, and the application of numerous burners have been proposed. Apart from the WA plasma jet, use was made of radio-frequency, hybrid, and microwave types of plasma. To increase the plasma volume, the plasma burners were arranged as described in Ref. [11].

However, the coating deposition regimes in each of these reactors are quite similar to the regimes of deposition of special films. The type of coatings produced by TPCVD embraces rather thick films (> 10 μm), which are impossible to deposit at high rates by other means, because the material is not in the liquid phase at normal pressure. Examples of such coatings are provided by a diamond coating and an SiC coating. Thin films — epitaxial or film with a high degree of orientation, for instance, superconducting films with a high T_c or yttrium-stabilized zirconium films — are required for other purposes. The TPCVD method has attracted interest thanks to the superlattice properties of diamond, because the method has made it possible to attain higher linear film growth rates in comparison with all other methods used at present [12 – 14].

2.3 Powder synthesis with the aid of radio-frequency thermal plasma

Among the numerous methods employed to fabricate fine powders, the radio-frequency plasma synthesis of fine powders, especially of refractive materials, furnishes very high temperatures and strong temperature gradients, and is attractive and chemically simple.

Furthermore, the supersaturation of the vapor, which provides the driving force for particle condensation, is very strong, resulting in the production of ultrafine particles for a homogeneous nucleation (activation centers). Ceramic powders like coroids, nitrides, oxides, and solid melts are well synthesized in radio-frequency plasma reactors. Today, this technology is known as RF-plasma synthesis, whereby the RF plasma serves as the processing medium. To synthesize thin powders, use is made of the RF plasma produced as a result of high-intensity arcs (alternating or direct current) and high-frequency (radio- or microwave-frequency) discharges. The latest advances in the development of new reactors and process upgrade have allowed a significant quality improvement of the powders produced by the RF-plasma method. The improvements were realized due to the use of a radio-frequency, hybrid dc reactor [15], reactive submerged arcs (RSAs) [16], numerous plasma jets, and liquid injection plasma reactors with a counterflow. They are all aimed at attaining the maximum possible heating temperatures, the maximum intermixing, and the longest duration of the material presence in the plasma. To synthesize thin films, use is made of either the discharge itself or the plasma plume of the discharge along the flow. The reagents in the plasma RF discharge may be gases, liquids, or solid substances prior to their injection into the plasma. For metals, however, the source gaseous phase is strictly limited. That is why the reagents most frequently employed in high-temperature plasma synthesis are solid substances. A liquid injection method was developed several years ago, which allowed overcoming the difficulties associated with the injection of solid materials, with the result that gaseous reagents gained advantage [17].

In this instance, a conventional radio-frequency plasma burner produces a high-temperature plasma jet of a rare gas, as a rule. The ionized source material in the liquid state is injected through an opening located opposite the plasma jet. The source material is in the form of a fine mist traveling in the direction opposite to the plasma jet, with the result that a permanently circulating vortex flow forms. This constant circulation increases the duration of the presence of the starting material in the relatively hot zone to ensure its complete vaporization and dissociation. The rapidly cooling flow issuing from the hot zone causes the supersaturation of the dissociated vapor of the source material, which in turn results in the attainment of the desired chemical composition and the production of fine powder particles by way of homogeneization. The powder accumulates in the water-cooled collector chamber and on the filter located at the outlet from this chamber. The same basic principle is also used in other reactors and other liquid feedstock.

The majority of earlier work on oxide synthesis was carried out on binary compounds. For many years, the large-scale production of TiO_2 (a pigment) was effected with arc gaseous heaters of the megawatt range.

During the past 12 years, with the progress of liquid-injection plasma synthesis technology with the aid of dc and RF plasma, it has been possible to synthesize multicomponent (three-, four-component, and more) solid oxide solutions, including aluminites, 'ferugits', and chromites [17 – 20], as well as high-temperature oxide superconductors [17, 21 – 25]. Apart from the production of 'exotic' oxide compounds, the sphere of application of thermal plasma synthesis of oxides has been minimal.

At the same time, a serious and sustained effort went into developing the RF-plasma synthesis of nonoxide ceramic powders. Considerable interest was shown in nitrides, then carbides, and lastly borides. The reagents employed most widely for the RF-plasma synthesis of nonoxide ceramics are hard materials and halides. To obtain pure ultrafine powders of ceramic materials, electroarc and nonelectrode radio-frequency plasma reactors were developed. A good showing was made by new plasma reactors that used multiple burners or combined and generated dc and RF plasmas, as well as by new approaches to the realization of synthesis. For more details, see the investigation reported in Ref. [26].

Those materials whose structure is made up of particles ranging in size from several to several dozen nanometers exhibit properties that are substantially different from the properties of the same materials with a higher grain size [27]. An example of these distinctions is provided by a higher hardness, improved plasticity, and also peculiar optical and electronic properties of the materials. A radio-frequency plasma synthesis is an efficient method of generating ultrafine particles, as noted above. The cooling rates in plasma generators are the crucial parameter, which determines the dynamics of particle production and growth [28].

Grishick and Chiu [29] described experiments in which the plasma-bearing source material in the vaporous state

expanded through a supersonic nozzle with a heated ceramic wall. This system implies the configuration of a one-dimensional flow with one-dimensional temperature gradients along the nozzle flow, which results in a high uniformity of the cooling rate. In addition, the employment of a nozzle furnishes higher cooling rates than other methods. With the aid of this system, it has been possible to synthesize ultrafine SiC particles (using $SiCl_4$ and CH_4 as the reagents). According to experimental data, the particles thus produced exhibit narrow distribution peaks of the order of several nanometers. The average diameter of SiC and Si particles measured about 8.5 nm, and 90% of the particles were under 16 nm in diameter [30].

2.4 Production of pulsed plasma jets

At the end of the 20th and early in the 21st century, there formed a new direction in the use of thermal plasmas — pulsed plasma detonation technology. This technology furnishes high coating quality and high deposition rates, is higher in efficiency due to the pulsed nature of deposition and low reagents consumption, and enhances the capabilities in the solution of basic and applied problems.

The modern technique of high-quality coating deposition follows the path of developing methods that provide a high speed of the material being deposited through the use of detonation devices [30, 31], rocket combustion chambers of different types [32, 33], and electromagnetic railotrons [34, 36].

Research shows [37] that having velocities of metal-based alloy particles up to 600 – 1000 m s^{-1} would suffice to produce a dense coating with a good adherence to the surface of an article even without heating.

In devices where the high-speed jet of combustion products is produced in rocket combustion chambers, no less than 10 m^3 of gas is expended to deposit 1 kg of tungsten carbide-based coatings [33]. The highest velocity of particles 45 ± 10 μm in diameter amounts to 600 – 650 m s^{-1}. 30 – 150 m ^{3} h^{-1} of combustible mixture goes to form a high-speed flow of combustion products in combustion chambers (CCs). However, the coating production rate and the coating quality do not grow, as a rule, in proportion to the thermal power [32]. The large volume of combustion gaseous mixture components is required, generally speaking, only to produce the high-speed jet of combustion products, but the problem of uniform powder material distribution over the jet section has not been solved, and therefore the problem of efficient use of energy remains to be solved.

Electromagnetic methods of powder acceleration and heating are under development [34 – 46]. In electromagnetic railotron-type accelerators, the acceleration and heating of the working gas and the powder are effected under the action of ponderomotive forces emerging in the passage of current through the electrodes (rails) and the conducting gas layer (plasma). The energy transferred to the plasma is proportional to the current strength. To attain a velocity of 2 – 4 km s^{-1} requires a current strength of 150 kA. In this case, the duration of acceleration is equal to 120 μs and the plasma temperature amounts to 20,000 °C [38].

A more successful type of railotron employed for coating deposition was proposed in Refs [34 – 36]. The velocity of the plasma 'piston' in this axial railotron ranges up to 10 km s^{-1} for a current strength of 20 kA. At the railotron output, the plasma velocity amounts to 4 km s^{-1}, which provides the powder acceleration and the production of a high-quality coating on the basis of tungsten carbides and aluminum oxides.

The arc localization in the plasma layer (piston) and the erosion of electrodes (rails) limit the range of applicability of electromagnetic systems. Moreover, they use complex devices for switching 20 – 150 kA electric currents with the repetition rate 2 – 10 Hz, which limits their reliability and operability.

Gas detonation systems intended for a coating deposition [30 – 32, 39] furnish the velocity of deposited powders up to 1000 m s^{-1} and their heating to the melting temperature at the same productivity as rocket combustion chamber-based devices, but have a thermal power dozens of times lower. The high-speed gas jet in detonation devices is formed through the realization of a detonation combustion regime and is independent of the volume of combustible mixture. Despite these advantages, the detonation coating deposition technology does not enjoy wide use owing to the complexity of the devices intended for dosing and feeding the powder material. In addition, the detonation devices are limited in the power of a unit pulsed jet of combustion products, which lowers the reliability of the coating deposition technology.

The known detonation devices intended for coating deposition [30, 31, 35, 36, 40] differ primarily by the method of feeding the powder being deposited and the gases into the combustion chamber. Devices have been built for coating deposition employing a side powder feed and gas-dynamic control systems [39]. The gases and the powder are introduced into the combustion chamber periodically on the lowering of pressure following the ejection of the high-speed jet of combustion products.

2.5 Description of the method of high-energy plasma jet production

Of all the known equipment employed to produce pulsed plasma jets, one can mark out accelerators with railotron and coaxial geometries, which are most efficient for surface modification and coating. The experimental and theoretical investigation of pulsed accelerators with railotron and coaxial geometries is adequately represented in monograph Ref. [36].

A new direction in the technology of surface modification and coating is presently being developed, which relies on electromagnetic accelerators of the combustion products of combustible gaseous mixtures [41 – 48].

Tyurin and Pogrebnyak [31] (Fig. 4a) came up with the idea of mixing the combustible mixture components and initiating detonation in a special chamber *1* located outside the pulsed plasma generation device — a plasmatron. The plasmatron consists of an inner conic electrode *2* and an outer electrode-cathode *3*. By the use of high-voltage source *5*, an electric field E is induced in the interelectrode gap *4* of width l between the two coaxial electrodes. An expendable metal rod *6* is built into the central electrode. The rod is, as a rule, made of refractory metals and alloys. The pulsed plasmatron contains a barrel intended for accelerating and heating the powder. The barrel length H is selected depending on the elemental composition and dispersion of the powder. For the deposition of a hard alloy, the barrel length is $H = 300$ mm. The powder is blown into the barrel through piping *8*.

The components of combustible gaseous mixture are fed to the detonation chamber *1*. The mixture's detonation is initiated upon their mixing. The combustion products are then delivered from the detonation chamber *1* to the interelectrode gap *4* and close the electric circuit of a source *5*. The electrically conducting layer of combustion products is

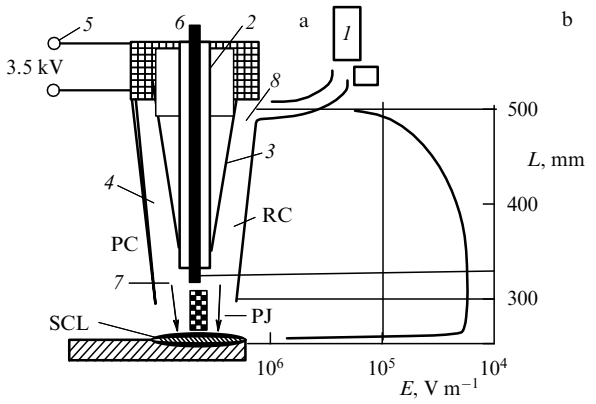

Figure 4. Schematic of a pulsed plasma device invoking the electromagnetic principle of introducing additional energy: (a) diagram of a plasmatron for producing a pulsed plasma jet: PC — plasma channel, SCL — shock-compressed layer, PJ — plasma jet, RC — reaction chamber; plot of electric intensity variation (L is the RC length).

accelerated under the action of gas-dynamic and electromagnetic forces. The powder introduced into barrel *7* is heated and accelerated by the pulsed plasma. The metallic expendable rod *6* vaporizes on heating to feed the doping elements into the plasma jet. When the pulsed plasma jet is ejected from the plasmatron, it closes the electric circuit between the electrode (anode) and the surface of an article (cathode). As a result of electric current passage through this jet, a pulsed magnetic field is formed, and the plasma and the powder are also heated due to Joule heat release.

The energy parameters of a pulsed plasma are determined through solution of the well-known two-dimensional transient propagation problem of a detonation wave (DW) in the electric field between two coaxial bodies of revolution (electrodes). This problem was simplified, and the average temperature, velocity, pressure, and combustion product density values along the axis of the working chamber (WC) were obtained neglecting the variation of its cross section [49, 50].

The geometric and energy parameters of the two-dimensional transient DW propagation problem were averaged over the interelectrode gap width of the WC as

$$\langle X\rangle = \frac{1}{h}\int_0^h X\,\mathrm{d}h\,, \tag{1}$$

where X takes the values $B, E, j, w, \ldots$; h is the averaged width of the annular gap; B is the magnetic induction; E is the electric field strength; j is the electric current; and w is the plasma flow velocity.

Integration of expression (1) was performed along the normal to the electrode surface. The calculated parameters depended only on the time and the distance along the WC generatrix to the point of DW initiation, denoted by l. The WC length is taken to be equal to L. In the approximation adopted, the position of the DW front is characterized by the function $l = l_{\mathrm{D}}(t)$ and the DW velocity by the equality $D = \mathrm{d}l_{\mathrm{D}}/\mathrm{d}t$. The surface of the DW front was divided into segments normal to the surface of the WC electrodes. The DW gain is determined from the equation

$$\mathrm{M_D} = \frac{D}{a_0} = \frac{1}{a_0}\,\frac{\mathrm{d}l_{\mathrm{D}}}{\mathrm{d}t}\,, \tag{2}$$

where a_0 is the energy gain in the DW owing to the input of electromagnetic energy.

We assume that the electric current $\langle j\rangle$ and field strength $\langle E\rangle$ vectors are perpendicular to the generatrix of the electrode surface and the plasma jet velocity vector $\langle w\rangle$ is parallel to it. The substantiation lies with the narrowness of the interelectrode gap ($h = 6-8$ mm) [51].

The gas flow in the channel behind the detonation wave is described by a system of partial differential equations with the inclusion of geometric parameters of the WC: the WC length L, the area of the annular gap section A, and the angle β between the conic generatrices of the WC electrodes. To calculate the parameters at the DW as a function of the distance l it travels, we use Whitham's method [52]. The DW Mach number $\mathrm{M_D} = \mathrm{M_D}\,(l)$ is defined by the solution of the differential equation with the inclusion of the integration constant (the acoustic characteristic c^+). The gas-dynamic parameters are expressed in terms of the Mach number of a stationary DW. We combine the equations of gas dynamics to obtain the system of equations

$$\frac{\mathrm{d}P}{\mathrm{d}l} + \rho a\,\frac{\mathrm{d}w}{\mathrm{d}l} = \frac{j_h}{w+a}\left(\frac{\gamma-1}{\sigma}\,j_h + \frac{a}{c}\,B\right) - \frac{\gamma P w}{w+a}\,\frac{1}{A}\,\frac{\mathrm{d}A}{\mathrm{d}l}\,, \tag{3}$$

$$(w+a)\,\frac{\mathrm{d}}{\mathrm{d}l} = \frac{\partial}{\partial l} + (w+a)\,\frac{\partial}{\partial l}\,, \tag{4}$$

where γ is the adiabatic exponent of combustion products; P and ρ are the pressure and the density; w is the average value of gas velocity behind the DW; a is the energy gain of the gas behind the DW due to the input of electromagnetic energy; j_h is the electric current; σ is the plasma conductivity; c is the dimensionless constant related to the total density of positive ions; and l the current length of the WC.

The following parameter values are substituted in the equations: $B = 0$, $j_h = \sigma E_0$. Here, E_0 is the averaged electric field strength vector in front of the DW. It is equal to the potential difference across the electrodes divided by the width of the annular gap.

We introduce new dimensionless variables Z and x in lieu of M_{D} and l:

$$Z = \sqrt{1 - \frac{\mathrm{M}_j^2}{\mathrm{M}_{\mathrm{D}}^2}}\,, \qquad x = \frac{l}{L}\,. \tag{5}$$

From the known value $Z = Z(x)$, we find formulas for the calculation of gas-dynamic parameters behind the DW:

$$D = \frac{a_0\mathrm{M}_j}{\sqrt{1-Z^2}}\,, \tag{6}$$

$$P = \frac{P_0\mathrm{M}_j^2\gamma}{(\gamma+1)(1-Z)}\,, \tag{7}$$

$$\rho = \frac{\rho_0(\gamma+1)}{\gamma-Z}\,, \tag{8}$$

$$U = \frac{\mathrm{M}_j a_0}{\gamma+1}\sqrt{(1+Z)(1-Z)}\,, \tag{9}$$

$$T = \frac{T_0\mathrm{M}_j^2(\gamma-Z)}{(\gamma+1)^2(1-Z)}\,. \tag{10}$$

In formulas (5)–(10), $\mathrm{M_D}$ is the detonation Mach number, P is the pressure, ρ is the plasma density, U is the total

velocity, T and T_0 are the respective plasma temperatures upon enhancement by electromagnetic field and without the field. The function $Z(x)$ is determined by solving the ordinary differential equation

$$l\left(1+Z+\sqrt{\gamma(\gamma-Z)(1+Z)}\right)\frac{\mathrm{d}Z}{\mathrm{d}x} = K(1-Z)^2\sqrt{1-Z^2}-\gamma(1-Z^2)\frac{1}{A}\frac{\mathrm{d}A}{\mathrm{d}x}, \quad (11)$$

where

$$l=\sqrt{\frac{\gamma}{(\gamma-Z)(1+Z)}},$$

which is integrated in elementary functions.

In the calculation of the geometric parameters of a pulsed plasmatron, we take $\gamma = 1.2$ the adiabatic index of combustion products; $\mathrm{M}_j = 5.0$ the Mach number of a stationary DW; $\rho_0 = 1$ kg m^{-3} the initial density of combustion products; and $E_0 = 35$ V m^{-1} the electric field strength in the interelectrode gap. $A = A(l)$ is the total area of the annular gap perpendicular to the WC axis.

We perform numerical integration of the ordinary differential equation subject to the initial conditions $Z(x) = 0$. The solution $Z(x)$ is represented in implicit form.

We write the solution of Eqn (11) as a formula for calculating the energy gain coefficient. For $\mathrm{d}A/\mathrm{d}x = 0$, the parameter K is a scaling parameter,

$$K=\frac{\delta E_0^2(\gamma-1)(\gamma+1)^2 L}{\gamma a_0\rho_0\mathrm{M}_j^3}, \quad (12)$$

where

$$\delta = c\,\frac{(kT)^{3/2}}{e^2\ln\Delta\sqrt{8\pi m_\mathrm{e}}}. \quad (13)$$

Here, k is the Boltzmann constant; t is the temperature; m_e and e are the electron mass and charge; and $\ln\Delta$ is the Coulomb logarithm, whose value depends on the temperature and the degree of plasma ionization in the WC.

In the numerical integration, we neglect the variability of $\ln\Delta$ and put $\ln\Delta = 10$. We also assume that the cross section of the annular gap is invariable, $\mathrm{d}A/\mathrm{d}x = 0$, and $E_0 = 35$ V m^{-1}. The resultant formula for the scaling parameter is

$$K = K_0\,\frac{(\gamma-Z)^{3/2}}{(1-Z)^{3/2}}. \quad (14)$$

The calculated distribution of the increase in the temperature T and the Mach numbers M_j and M_D of the gas behind the detonation wave front over the length of the interelectrode gap of the reaction chamber l/L for different values of the electric field strength E corresponds to the observed one, and when $l/L \approx 1$, the maximum temperature is equal to about 3.0×10^4 K for the gap length about 40 mm. The plasma jet energy increases nonlinearly. Its peak values are reached at the plasmatron output.

An analysis of formulas (6)–(14) shows that the temperature, the pressure, the velocity, and the density of the pulsed plasma jet can be varied within wide limits. These parameters depend on the WC length, the cone angle, the interelectrode gap width, and the electric field strength.

The results of numerical integration of the ordinary differential equation showed that increasing E_0 engages the second factor in DW acceleration — the release of Joule heat. We assume that the conductivity behind the DW is due to the electrons. In this case, the acceleration of the wave is accompanied by a temperature increase, which in turn leads to an increase in the velocity and the density of the plasma jet. The field intensity in the WC decreases lengthwise of the plasma piston motion, which is related to the lowering of the voltage across the capacitor plates and the broadening of the interelectrode gap, with the conductivity of the plasma layer increasing in this case. This stabilizes the consumption of energy from the converter capacitors and ensures the smoothness of energy input into the DW. For the initial electric field strength above 100 V m^{-1}, the rate of plasma conductivity growth is high and 100 mm of the WC length are sufficient for its breakdown by electric discharge to occur.

The energy characteristics of the pulsed plasma jet are most efficiently controlled by the length of the working chamber. By varying the WC length, it is possible to obtain the following technological characteristics of the pulsed plasma: the jet power density in the range between 10^4 and 10^7 W cm^{-2}, the temperature from 5×10^3 to 3×10^4 K, and the velocity from 2000 to 8000 m s^{-1}. The highest energy of the plasma jet in a plasmatron are attained for a WC length exceeding 0.5 m.

According to the results of investigations conducted, the plasma jet velocity changes only slightly when the WC length is varied between 0.3 and 0.5 m, which was taken into consideration when optimizing the dimensions of a plasmatron intended for coating deposition. The pulsed plasmatron [39, 40, 49] is intended for modifying the surface of articles and for gas-thermal deposition of high-quality coatings of metals, hard alloys, and metal oxides.

The components of combustible mixture and powder materials are continuously fed to the plasmatron, which reduces the price of the coating technology and the technological devices.

3. Modification of the properties of metals, alloys, and surface layer hardening using a pulsed plasma jet

3.1 Doping and mass transfer due to the action of a pulsed high-speed jet

The authors of Ref. [53] doped α-Fe with the aid of an Mo electrode in the processing by a pulsed high-speed jet. The parameters of sample processing regimes are collected in Table 1.

An X-ray phase analysis suggests that the main phase upon exposure is SCC-Fe (the space-centered crystal lattice with $d = 2.866$), and there additionally forms the Fe_7Mo_6 phase with the lattice parameters 2.157 (2.15); 2.086 (2.08); 1.811 (1.80), and the FeMo phase with the parameters 2.157

Table 1. Sample processing regimes.

Number	Material	Number of pulses	Distance, mm	Frequency, Hz	Depth, mm	Capacitance, μF
1	α-Fe	4	40	1.5	30	800
2	α-Fe	10	40	1.5	30	800
3	α-Fe	15	40	1.5	30	800
4	α-Fe	20	40	1.5	30	800

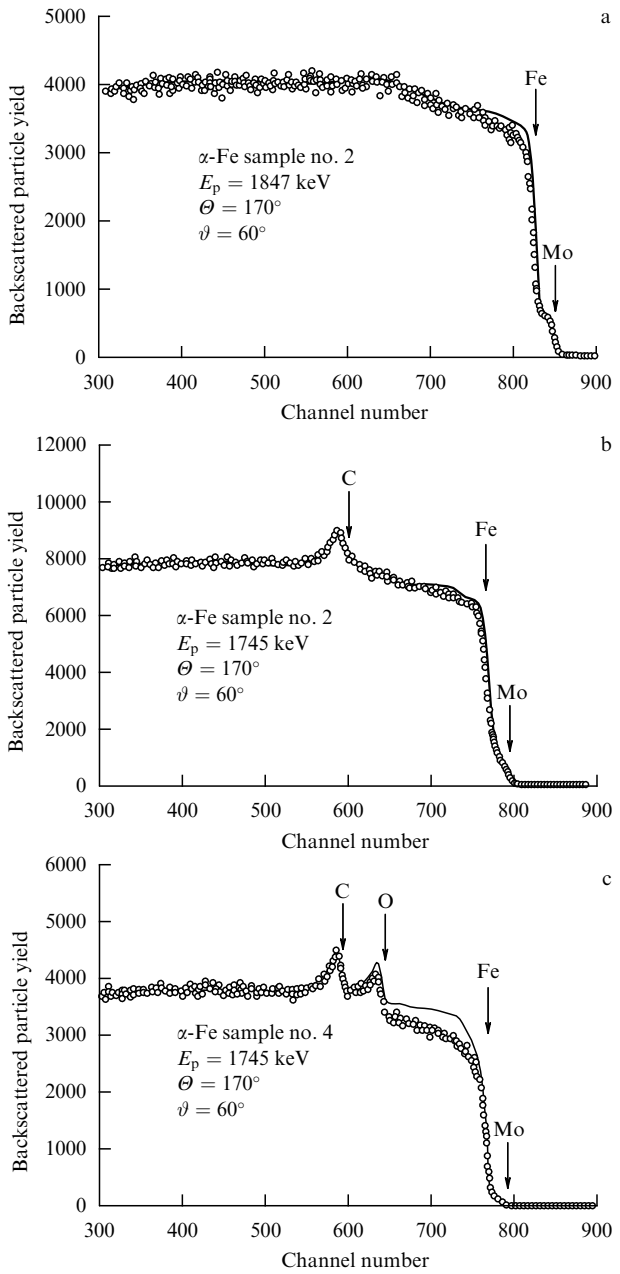

Figure 5. (a) Energy spectrum of Rutherford backscattering obtained with the use of $^4He^+$ with the energy 1847 keV for an α-Fe sample after pulsed plasma processing (10 pulses, $\Theta = 170°$, $\vartheta = 60°$); (b) energy spectrum obtained by the method of elastic resonance of $E_p = 1745$ keV protons for determining carbon and nitrogen densities for an α-Fe sample (the same regime); (c) energy spectrum obtained by the method of elastic resonance of $E_p = 1745$ keV protons for determining carbon and oxygen densities for an α-Fe sample processed by the pulsed plasma jet (20 pulses).

(2.14); 2.086 (2.09) is possible (the data in parentheses were borrowed from a reference book).

Figure 5 shows the energy spectra of Rutherford ion backscattering obtained for α-Fe upon exposure to the plasma jet (a) and the spectra of elastic resonance with protons in the region $E_p = 1745$ K (b) obtained for the same sample. In the spectrum in Fig. 5a, one can see the (kinetic factor) boundary for Fe and for Mo, the spectrum broadening in the lower part on the right side, while the formation of a small shelf is an indication that a $FeMo_2$ compound in a surface layer approximately 300 nm in thickness forms. Furthermore, a carbon peak is clearly seen in the spectrum obtained using the proton resonance.

Figure 5c also shows the spectrum of elastic resonance with protons for an Fe sample processed with a larger number of pulses. Referring to the spectrum, along with the growth of carbon and nitrogen densities in the surface layer, oxygen density near the surface increases (about 40 at. %). A further increase in the number of pulses leads to a still greater increase in the oxygen density at the surface. A different picture is observed for the doping element (the product of erosion and vaporization of the electrode). The density of Mo was found to be highest near the surface (i.e., in the layer up to 10 μm in thickness). For 10 pulses, the limiting Mo density is equal to about 8 at. %, and its peak is located at the depth about 7 μm from the surface.

The carbon density was shown to increase only slightly with the number of pulses, while the oxygen density was shown to amount to 40 at. % even after 15 pulses. The surface layer doping with Mo passes through a maximum when the number of pulses is increased from 4 to 20, attaining the peak density about 8 at. % upon exposure of the α-Fe surface to 10 pulses of the high-speed pulsed jet.

Analyzing the structure of a transverse metallographic section of the α-Fe sample, the authors call attention to the fact that the flowed layer thickness amounts to 50 μm upon exposure to 10 plasma jet pulses.

Therefore, the authors of Ref. [53] showed that employing a plasmatron with an eroding Mo electrode makes it possible to dope the surface layer to a depth of at least 10 μm and to saturate (dope) the surface layer of the sample not only with Mo but also with oxygen and carbon, as well as to fuse the surface layer having a thickness much deeper than the doped region.

3.2 Face-hardening and modification of titanium alloys employing pulsed plasma technologies

The authors of Ref. [54] investigated the efficiency of pulsed-plasma processing with samples of technical titanium VT1-0 and its alloys VT6, VT23, and VT22 using the X-ray structural analysis method, scanning electron microscopy (SEM), and secondary ion mass spectrometry; they also measured microhardness with a diamond Vickers pyramid [54].

X-ray phase analysis showed that the VT1-0 type titanium samples in the initial state contain only the α-phase of Ti, and the VT6, VT22, and VT23 alloys additionally contain the β-phase of Ti. On the surfaces of all alloys, there is an oxide film, primarily of the natural oxide TiO_2 (rutile), which is a barrier to further oxygen diffusion inside the coating [55]. Secondary ion mass spectrometry (SIMS) clearly shows TiO^+ and TiO peaks.

Pulsed plasma processing (PPP) of technically pure titanium in the mode of fusion by six pulses with the specific power ~ 1 MW cm^{-2} has led to significant structural-phase changes in the surface layer. Comparing the diffraction patterns recorded for VT1-0 titanium samples in the initial state and after the PPP reveals significant changes in the latter. First, δ-TiN, ε_1-Ti_2N, ε_3-Ti_3N, and TiC interference lines appear, testifying to the production of nitride and carbide phases (Figs 6a – 6e). The presence of titanium carbides and nitrides was also recorded with the SIMS technique. Considering the blur of the interference lines and the presence of δ-TiN and TiC in significant amounts, it may be suggested that a solid solution of nitrogen and carbon in α-Ti was formed.

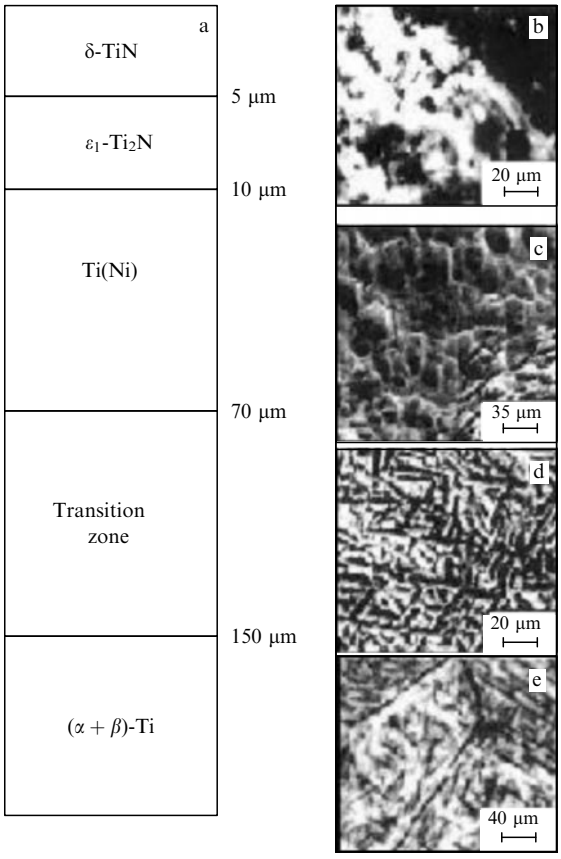

Figure 6. Structure of the nitrated surface layer of the VT6 alloy: (a) conventional diagram of the structure, (b) SEM image of the zone of the solid solution of nitrogen in titanium, (c) general structure of the nitrated layer, (d) transition zone, (d) base.

Second, owing to the erosion of the expendable molybdenum electrode in the course of PPP, implantation of molybdenum and molybdenum nitride occurred, which was produced in the plasma jet due to the molybdenum – nitrogen interaction, into the surface of the titanium. Molybdenum (β-stabilizer) did not dissolve in the titanium but persisted in the form of separate inclusions, which is attested to by the emergence of Mo and Mo_2N peaks in the diffraction pattern.

Third, the intensity of TiO_2 ('anagas') peaks increased two-fold and that of TiO_2 (rutile) peaks increased insignificantly.

In comparison with the initial state, the PPP of the VT6 alloy in the surface fusion mode resulted in the disappearance of the peak corresponding to the β-phase, which testifies to the saturation of the matrix material with the α-stabilizing elements N, C, and O, which are plasma components. The after-PPP diffraction pattern of the VT6 alloy differs from a similar VT1-0 titanium diffraction pattern by the absence of the peaks corresponding to the phase ε_3-Ti_3N. The ε_3-Ti_3N phase formation in the VT6 alloy was recorded only after 15-pulse processing.

The PPP of the VT6 alloy in the mode without surface fusion resulted in surface layer saturation with plasma components (N, O) due to thermal diffusion and plasma impact, which affected the production of carbide and nitride phases. The depth-nonuniform cooling of the sample favored the production of the martensitic α'- and α''-phases. On the alloy surface, there are two kinds of δ-TiN: porous dark-colored and continuous golden-yellow with the total thickness less than 1 μm. Located under this layer is a layer of the ε_1-Ti_2N phase. The total thickness of the layer modified under this plasma processing mode does not exceed several micrometers. These structural-phase changes gave rise to an insignificant increase in the microhardness of the VT6 alloy (1.1-fold).

In the VT22 alloy, after PPP (1 pulse), the α-Ti peaks disappeared almost completely and the β-phase peaks increased in intensity. The PPP of this alloy in the surface fusion mode resulted in the formation of a nearly 100% β-phase, with the understanding that the interstitial phase is disregarded. This is not surprising, because the β-stabilization coefficient $K_\beta = C/C_{\min}$ (C is the β-stabilizer density in the alloy and $C_{\min}$ is the minimal density whereby an alloy from the β-domain can acquire a 100% β-structure) for this alloy is equal to 1.05 [56]. In this case, the β-phase peaks become more blurred, which also testifies to VT22-alloy saturation with plasma components. There additionally appeared medium-intensity (200) δ-TiN and (112) ε_1-Ti_2N peaks and low-intensity TiC peaks. The diffraction patterns obtained for the VT23 alloy after plasma processing differ from the VT22-alloy diffraction pattern by a higher intensity of the δ-Ti, δ-TiN, ε_1-Ti_2N, and TiC peaks.

The sectional X-ray structural analysis of an angle lap with the aid of a scanning electron microscope showed that the modified surface is layered in structure. Located at the surface is structurally fine-grained δ-TiN up to several micrometers in thickness, beneath it are a thin ε_1-Ti_2N layer and the zone of a solid solution of nitrogen in titanium. This zone consists of oval grains both for pure α-Ti (the VT1-0 alloy) and for (α + β)-Ti (the VT6, VT23, and VT22 alloys). The nitrated zone thickness depends on the alloy grade. The more β-phase contained in the initial state of the alloy, the thinner the modified layer. The SEM data suggest that in α + β alloys (VT6, VT22, VT23), unlike in technically pure titanium, a transition zone in the form of morphologically lamellar grains was formed between the gas-saturated layer and the base metal. Considering the lamellar grains structure of this zone, which is characteristic of the α-phase of titanium, and the presence of martensite, which was discovered in the VT6 alloy upon PPP in the mode without surface fusion, the authors came to believe that the transition zone may be a martensite phase.

To elucidate the effect of the number of pulses on phase formation in the PPP, an investigation was made of VT6 alloy samples processed by a different number of pulses (1, 5, 10, and 15 pulses). The fuzziness of interference line peaks decreases with an increase in the number of pulses. The intensity of α-phase lines also decreases, while the δ-TiN and TiC line intensities increase. The decrease in α-Ti line fuzziness and the growth of the intensities of the interference lines δ-TiN and TiC with the number of pulses is attributable to the transition of nitrogen and carbon from the 'free' state to the bound state, i.e., to the formation of titanium nitride and carbide.

Most likely, the growth of nitrides and carbides on the surface depends on the diffusion rate of the saturating element and is determined primarily by the temperature and by the duration and the number of pulses. The presence of oxygen substantially accelerates the diffusion of nitrogen [56]. The total content of nitrogen in the bound state (δ-TiN) in the surface layer rises up to 40 at. % with an increase in the number of pulses.

Table 2. Microhardness of titanium alloys.

Alloy	Composition	State	Microhardness, GPa
VT1-0	99.46% Ti (technical titanium)	Initial	2.576 ± 0.011
		PPP by 2 pulses with fusion	6.649 ± 0.014
		PPP by 6 pulses with fusion	9.103 ± 0.017
VT6	Ti-6%Al-4%V	Initial	3.696 ± 0.010
		PPP by 6 pulses without fusion	4.084 ± 0.012
		PPP by 1 pulse with fusion	5.031 ± 0.011
		PPP by 5 pulses with fusion	6.288 ± 0.013
		PPP by 6 pulses with fusion	7.688 ± 0.017
		PPP by (5 + 5) pulses with fusion	7.353 ± 0.012
		PPP by (5 + 5 + 5) pulses with fusion	8.199 ± 0.015
VT23	Ti-5.5%Al-2%Mo-4%V-1%Cr – 1%Fe	Initial	3.425 ± 0.012
		PPP by 6 pulses with fusion	6.835 ± 0.015
VT22	Ti-5%Al-5%Mo-5%V-1%Cr – 1%Fe	Initial	4.161 ± 0.010
		PPP by 1 pulse with fusion	4.972 ± 0.016
		PPP by 3 pulses with fusion	5.031 ± 0.012
		PPP by 6 pulses with fusion	5.106 ± 0.014

A morphology investigation of the VT23 alloy upon PPP with two and six pulses performed using a scanning electron microscope showed that there forms a relief on the surface under irradiation. This relief has a characteristic morphology in the form of ordered valleys and peaks, which are oriented primarily across the motion of the plasma flowing along the surface. In the view of the authors of Ref. [56], this is attributable to the fact that individual shock waves, which are generated when the solid surface is exposed to the particle flux, collide inside the substrate to form local foci of increased pressure [57, 54].

In the surface relief investigation of the VT1-0 titanium and titanium alloys (VT6, VT23, VT22) upon PPP with a different number of pulses, it was established that the relief microgeometry is determined both by experimental conditions and by the type of alloy being processed. For instance, the VT23 alloy surface exposed to two-pulse PPP is corrugate and exhibits a small number of gas bubbles, while the VT1-0 titanium surface processed with two pulses is friable and porous, and exhibits a large number of gas bubbles. The three-pulse PPP of the VT22 alloy resulted in sputtering of the material over the surface.

Therefore, the surface relief of titanium alloys exposed to PPP may vary from wavy to porous and may even have the appearance of a sputtered droplet, depending on the type of titanium alloy, the number of pulses, and their intensity. In addition, the formation of a wavy relief gives rise to significant stress, which may lead to the formation of cracks.

The authors believe that pulsed plasma processing can provide excellent service properties (wear, heat, and corrosion resistances) in combination with improvement of plasticity and strength of the initial material.

In the microhardness measurements, when the load on titanium VT1-0 and its VT6, VT22, and VT23 alloys was equal to 50 G, no pyramidion imprints were detected on the surface, which is an indication of the high microhardness of the carbide and nitride surface layers. That is why the microhardness prior to and following the PPP was measured for a 200 G load. In this case, the thin carbide and nitride layers are pierced through. Here, the microhardness measurement refers primarily to the gas-saturated and transition zones of the initial material, although the carbide and nitride layers make their contribution to the integral microhardness magnitude.

Microhardness investigations (Table 2) showed that the maximum microhardness in the initial state is inherent in VT22 alloy samples and the minimal one in the samples of technically pure titanium VT1-0. A different picture is observed after PPP: the maximum microhardness is inherent in the samples of technically pure titanium VT1-0 processed with six pulses in the surface fusion mode and the minimal microhardness in the samples of the VT22 alloy. According to Refs [54, 56], the alloy strengthening efficiency in the domain of homogeneous α-solid solutions normally decreases with an increase in dissolved element content. This effect supposedly occurs because the dependence of mechanical properties of β-alloys on the density of alloying elements is described by a parabolic dependence rather than the linear one, and hence the capacity of the β-alloys to harden is exhausted for a high density of the alloying elements.

The PPP-induced rise in the microhardness of titanium alloys is most likely caused by the emergence of metastable martensite phases, the formation of titanium nitrides and carbides, and the increase in the defect density and the modified layer thickness.

3.3 Deposition of metal coatings on substrates

3.3.1 Coatings of SS 316 L stainless steel on a low-carbon steel substrate. Figure 7 shows the energy spectra of Rutherford $^4He^+$ ion backscattering (b) and elastic resonance with protons (a) for coated samples. One can see from the data obtained that the surface layer exhibits a substantial density of carbon and oxygen and an Mo peak is additionally observed. From the results of analysis, it was possible to determine the densities of elements in the surface coating layer up to 10 μm deep (Table 3). Referring to Table 3, the oxide layer thickness amounts to about 1.8 μm, the highest density of oxygen being about 40 at. % and of carbon about 18.5 at. %. In this case, if the well-known formula [58, 59] is used, the ratio between the O and Fe signals allows finding the oxide stoichiometry, which is close to Fe_3O_4. Also observed is redistribution of the dopant and a density lowering of Ni (to several percent) and Cr (from 3 to 8 at. % in a layer up to 1 μm in thickness).

Figure 8 shows clearly that the coating is nonuniform and is a mixture of domains with different susceptibilities to etching, i.e., with different chemical compositions. The

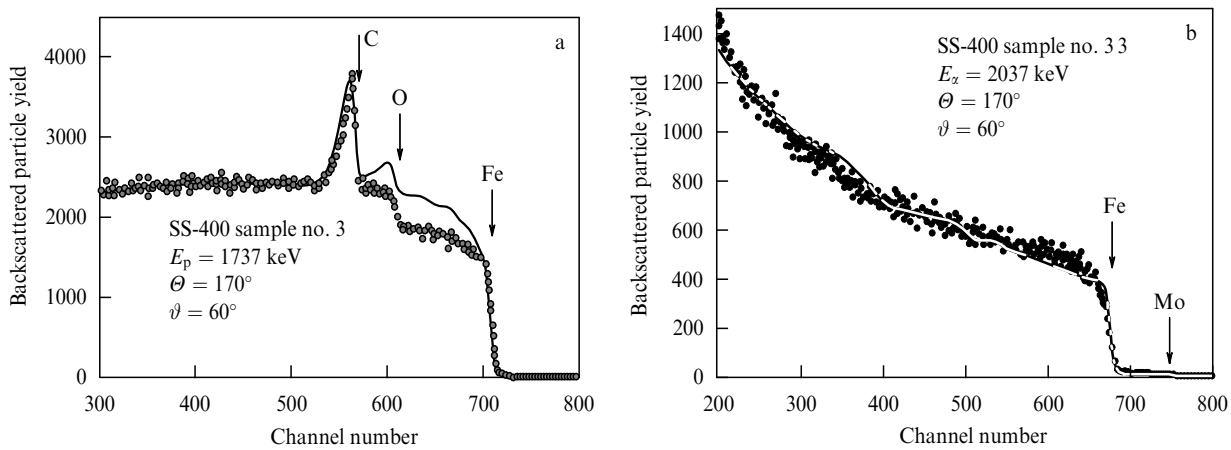

Figure 7. (a) Energy spectra measured for SS-400 steel samples with a coating of 316L stainless steel powder, an elastic resonance with $E_p = 1737$ keV protons, $\Theta = 170°$, $\vartheta = 60°$. (b) Energy spectra measured for SS-400 steel samples with a coating of 316L stainless steel powder with the aid of Rutherford backscattering for the same sample for $E_\alpha = 2037$ keV, $\Theta = 170°$, $\vartheta = 60°$.

Table 3. Elemental densities (at. %) in the coating of SS-316L.

Coating depth, mm	Mo	Ni	Fe	Cr	O	C
135.8	0.49	3.57	35.19	2.48	39.73	18.54
271.4	0.51	4.35	38.78	4.89	36.88	14.59
407.6	0.52	5.14	42.22	5.88	35.20	11.04
542.6	0.54	6.05	47.91	6.76	31.25	7.49
805.1	0.56	7.29	54.55	8.07	24.62	4.91
1298.4	0.59	8.95	63.51	13.56	11.11	2.28
1775.9	0.60	10.43	68.09	17.69	3.19	0.00
2716.0	0.60	10.44	71.06	17.90	0.00	0.00
4478.6	0.60	10.44	71.06	17.90	0.00	0.00
10,353.9	0.60	10.44	71.06	17.90	0.00	0.00

etched metallographic section structure of the SS-400 steel and the 316L coating is shown. Investigations showed that the coating – steel contact surface is highly irregular.

The SS-400 steel used as a substrate for the coating had a polycrystalline structure on the basis of α-Fe in the initial state. A substructure with chaotically distributed dislocations was observed inside ferrite grains in the majority of cases. The scalar dislocation density was 10^{10} cm^{-2}. In individual cases, a subgrain structure was present in ferrite grains. The steel under investigation belongs to two-phase materials — the second phase is cementite particles located inside the ferrite grains and along their boundaries.

Figure 9 depicts the structure of steel in the zone of its contact with the coating. As in the initial state, the steel has a two-phase structure, consisting of ferrite grains and cementite particles located inside the grains and along their boundaries. In the majority of cases, a dislocation structure in the form of cells is observed in the grains. The layer under analysis is in a stressed state.

This is confirmed by bend extinction contours observed in ferrite grains (see Fig. 9). Yet another feature of the state of steel in the zone of its contact with the coating is the presence of the second phase in ferrite grains in the form of numerous round-shaped particles ranging from 25 to 30 nm in size (see Fig. 9). Observed in the grains in this instance is a high dislocation density (7×10^{10} cm^{-2}). An analysis of the electron diffraction pattern (Fig. 9b) suggests that these particles are a carbide phase of the type Me_3C, $(Fe, Cr)_3C$.

The coating in the zone of its contact with steel has a nanocrystal structure. The crystallite dimensions vary between 4 and 25 nm (see Fig. 9). The small crystallite dimensions are also confirmed by the circular structure of the electron diffraction pattern obtained from this part of the sample. An analysis of electron diffraction patterns shows that the nanocrystallites are an Fe_3O_4 type oxide.

The near-surface layer located at the depth 5 – 10 μm from the free surface is formed by a polycrystalline phase on the basis of a solid solution of chromium and nickel in iron (Fe, Cr, Ni). The crystallite dimensions range from 0.1 to 0.3 μm.

The coating layer that lies 0.5 mm from the free surface contains a large number of particles of the $\sim Fe_3O_4$ type oxide phase located inside and at the boundaries of the crystallites of the phase (Fe, Cr, Ni). The particles are round-shaped and measure $\sim$ 25 nm on average. In individual cases, the oxide phase forms polycrystalline films with $\sim$ 2 nm sized crystallites. The coating layer, which lies on the free surface, is formed by the Fe_3O_4 type phase crystallite with dimensions lying in the 15 – 20 nm range. The small dimensions of the crystallites are also confirmed by the circular structure of electron diffraction patterns.

Therefore, the coating of the samples has a polycrystalline structure and the phase composition (Fe, Cr, Ni). The free surface and the layer that comes into contact with the steel are made of an oxide layer with a nanocrystalline structure. The steel in the contact zone is a polycrystalline aggregate; its crystallites exhibit a high density of dislocations at which carbide phase particles are located.

3.3.2 Investigation of the structure and properties of Ni-based Hastelloy C coatings. In Refs [58, 59], the authors investigated the structure and phase composition of a coating of Ni-based Hastelloy C.

Figure 10 shows the energy spectrum of elastic resonance with protons measured for coated samples. As is apparent from the resultant data, a substantial density of C and O is observed in the surface layer, which also involves admixtures of the following elements: W, Mo, Ni, Co, Fe, Mn, and Cr. An analysis yielded the elemental densities in the surface layer of the coating up to 10 μm in depth (Table 4).

One can also see from Table 4 that the density of oxygen and carbon in the vicinity of the surface is equal to about

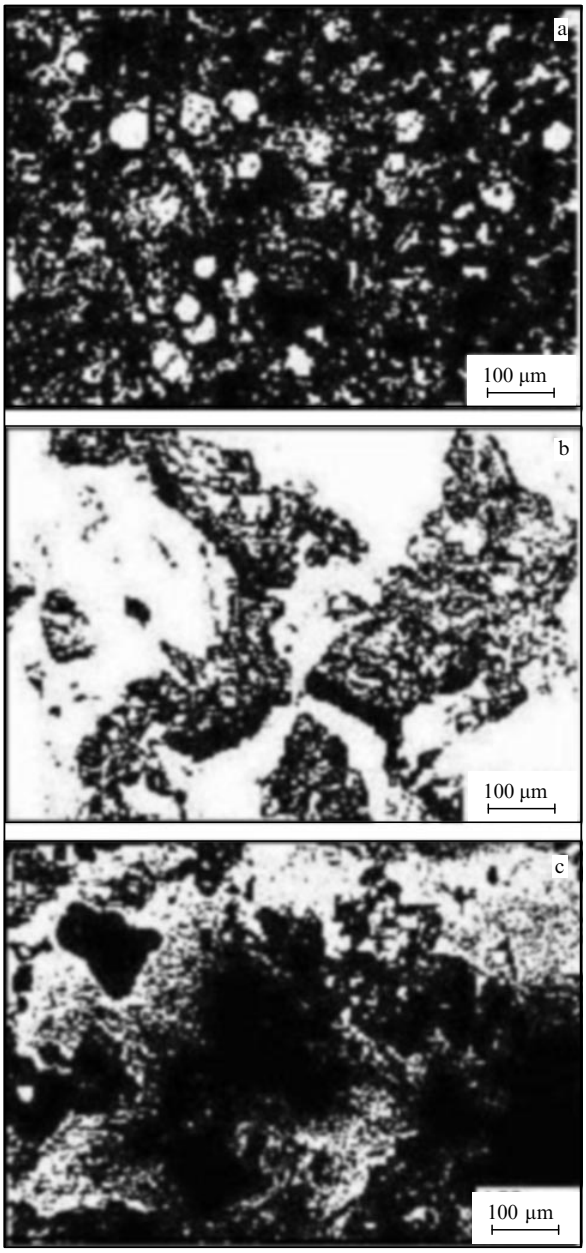

Figure 8. Metallography of an etched lateral section of SS-400 steel with a coating of SUS316L (dark areas — coating, light areas — SS-400 steel): (a) structure of the coating in a layer parallel to the free surface; (b) transverse section; (c) section made at the angle 1° – 3° to the surface.

25 at. %; the density of the remaining elements, the main components of the Hastelloy alloy, is significantly lower. The oxide film thickness is about 2 μm, and carbon and carbides reside within 1 μm from the surface.

In the majority of cases, inside the ferrite grains, it is possible to observe a substructure with randomly distributed dislocations. The scalar dislocation density is $\langle\rho\rangle \sim 2 \times 10^8$ cm^{-2}. In individual cases, the ferrite grains had a subgrain structure. The steel under investigation belonged to two-phase materials — the second phase being cementite particles located inside the ferrite grains and along their boundaries.

The steel is made up of ferrite grains, and observed inside the grains is a cellular dislocation substructure. The α-Fe reflexes are blurred, which may be indicative of the presence of a second phase. The SS-400 steel, which was employed as a substrate for the deposition of coatings, had an α-Fe-based polycrystalline structure in the initial state.

From the blur of {110}α-Fe type reflexes, it may be suggested that the phase (Fe, Cr, Ni) is present. Our attention is engaged by the cell boundaries — the edges are not robust, the boundaries are broadened, and the dislocations are indistinguishable. This may be testimony to the presence of interstitial impurities (oxygen, nitrogen, carbon) at the boundaries. Observed in individual grains is a dislocation structure in the form of chaos. In such grains, the scalar dislocation density is equal to $\sim 5 \times 10^{10}$ cm^{-2} and, as a rule, bend extinction contours are observed inside, implying a high stress level in the steel structure. Reflexes in the electron diffraction patterns recorded from such grains are stretched, which is indicative of an azimuthal misorientation of the structure elements. Along with the grains bearing a cellular dislocation substructure, there are ferrite grains with subgrains, whose average dimensions are 0.15 – 0.20 μm. A dislocation substructure in the form of lattices with $\langle\rho\rangle \sim 5 \times 10^{10}$ cm^{-2} is observed inside the subgrains. Located at the subgrain boundaries are domains with the second phase — molybdenum carbide α-$MoC_{0.54}$.

In the TEM-assisted investigation of the structure of the transition layer containing a section of the coating, one can see that the coating is structurally dispersed with crystallites measuring ~ 50 – 100 nm. The electron diffraction pattern recorded from such a two-layer portion of the foil shows reflexes of the phase (Fe, Cr, Ni).

An analysis of the data outlined shows that the coating is formed by grains with a nickel-based FCC lattice (judging by the chemical composition of the coating). Observed inside the grains is a dislocation substructure with the dislocation density $\sim 6 \times 10^{10}$ cm^{-2}. The light grain images are spotted. An analysis of electron diffraction patterns suggests that this contrast is due to nickel oxides. In individual cases, the grains exhibit a cellular dislocation substructure. The cells are misoriented as indicated by the azimuthal blur of reflexes in the electron diffraction pattern (Fig. 11). The cell boundaries are fuzzy, which testifies to the possible presence of an interstitial impurity at the cell boundaries.

In individual cases, spicular crystals are found in coating grains along their boundaries. An analysis of the electron diffraction patterns suggests that they are martensite crystals formed in the $\gamma \to \alpha$ martensite transformation of iron-, chromium-, and carbon-enriched parts of the coating. The martensite transformation is accompanied by the formation of coating regions with a high ($\sim 9 \times 10^{10}$ cm^{-2}) dislocation density.

The coating layer located at the depth ~ 1 μm from the free surface had a polycrystalline FCC structure. Seen inside the grains is a dislocation structure in the form of chaotically distributed dislocations with the density 6.5×10^{10} cm^{-2}, and individual grains exhibit a subgrain structure (see Fig. 11). The subgrains measure ~ 0.1 – 0.2 μm. The subgrains are not oriented, and the azimuthal component of the total misorientation angle amounts to ~ 6°. Coating domains with the crystal dimensions ~ 10 – 20 nm are sometimes encountered (see Fig. 11).

The free surface of the coating forms a multiphase structure on the basis of an FCC lattice, which contains numerous inclusions of nanometer-sized oxycarbide phases, with the crystallite dimensions equal to ~ 20 – 30 nm. This layer is thin and measures a fraction of a micrometer. As we

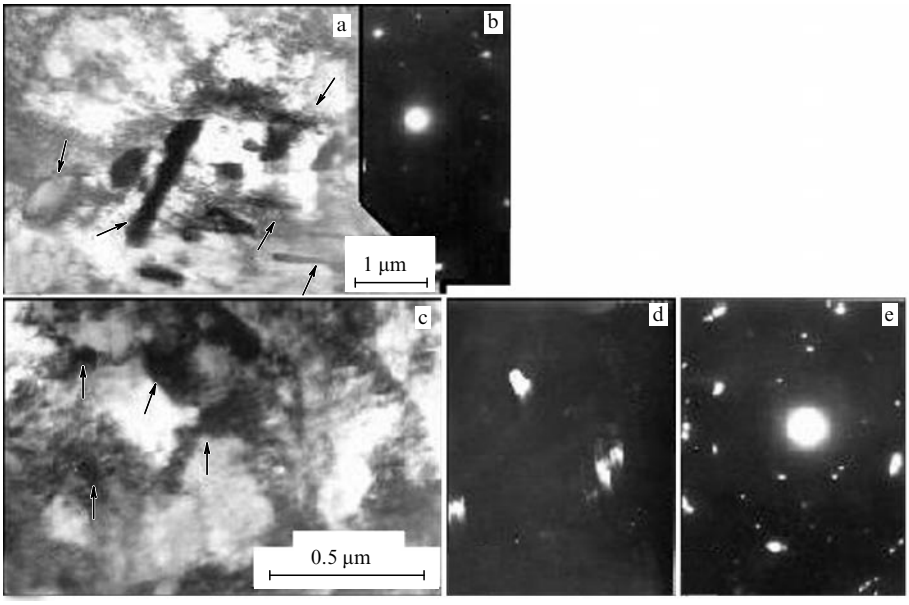

Figure 9. TEM image of the substrate (SS-400 steel) structure at the interface with a SUS316L stainless steel coating: (a, c) light-background image; (b) electron diffraction pattern to (a); (d) dark background in cementite reflex; (e) electron diffraction pattern to (c). Arrows indicate cementite particles.

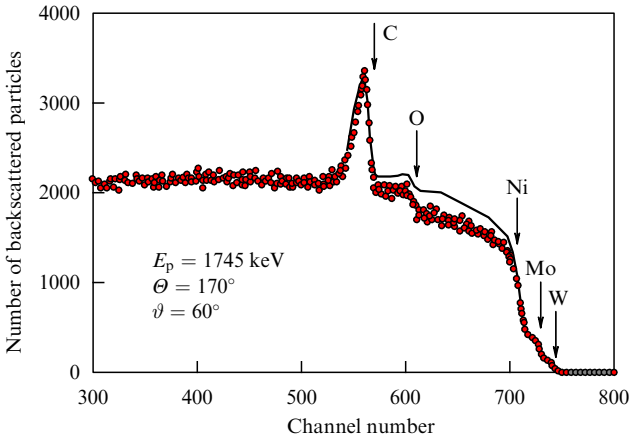

Figure 10. Energy spectrum of the elastic resonance with protons ($E_p = 1745$ keV, $\Theta = 170°$; $\vartheta = 60°$) measured for Hastelloy C coated samples.

Table 4. Elemental densities (at. %) in the Hastelloy C coating.

Coating depth, nm	W	Mo	Ni	Co	Fe	Mn	Cr	C	O
122.9	0.90	4.53	29.44	0.22	2.71	0.45	10.20	24.77	26.78
247.6	0.99	4.97	32.33	0.25	2.98	0.50	11.94	19.77	26.27
373.8	1.09	5.44	35.30	0.27	3.26	0.54	13.64	15.11	25.36
501.6	1.17	5.89	38.28	0.29	3.53	0.59	15.12	10.44	24.70
759.6	1.34	6.66	43.28	0.33	4.00	0.66	16.71	4.44	22.57
1014.8	1.52	7.61	49.50	0.39	4.57	0.76	17.13	0.36	18.15
1263.4	1.62	8.07	52.49	0.41	4.85	0.80	18.17	0.38	13.21
1734.4	1.86	9.33	60.66	0.46	5.60	0.94	18.35	0.00	2.80
2663.0	1.93	9.65	62.74	0.49	5.79	0.97	18.43	0.00	0.00
4404.2	1.93	9.65	62.74	0.49	5.79	0.97	18.43	0.00	0.00
10,208.2	1.93	9.65	62.74	0.49	5.79	0.97	18.43	0.00	0.00

recede from this layer towards the interior, the dimensions of oxycarbide inclusions increase to 60 nm and the density lowers.

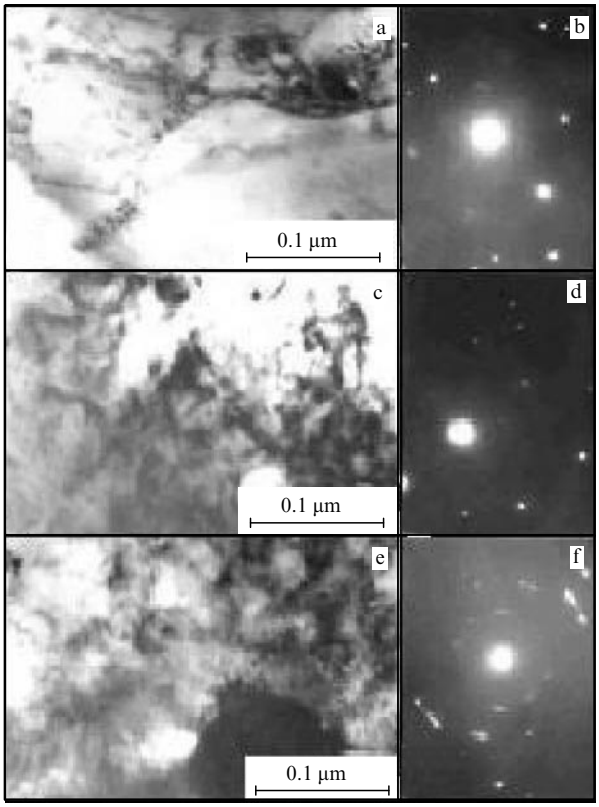

Figure 11. TEM image of a Hastelloy coating: (a, c, e) light background, (b, d, f) electron diffraction patterns (to these images).

Therefore, the coating that appears on a sample is formed by the polycrystalline phase with an FCC lattice (nickel-based solid solution). Located on the coating surface is a nanocrystalline oxide film of Fe_3O_4. With increasing the distance from the surface of the coating, the oxides become bigger, while their density lowers. No oxide sublayer was found in the coating – steel contact zone.

The photographs that demonstrate the structure of the coating and the surface steel layer were obtained from sections made at a low angle (3°) to the surface. In the coating – steel contact zone, one can clearly see a mixed structure consisting of coating isles in steel, which are widely diversified in shape and dimensions. The photograph of a transverse section of a Hastelloy coating shows clearly fused parts measuring about 40 – 50 μm; small pores are visible in the coating [48].

Corrosion tests were carried out by a procedure that was adequately described in Ref. [60], in sea water for Hastelloy coatings of various thickness. The resultant data suggest that the corrosion potential is minimal for 300 μm thick coatings, this potential lowering almost three-fold during the first hours in comparison with the potential of the SS-400 steel substrate. The corrosion resistance is better than in the case of thicker coatings: for a coating thickness of 300 μm, it is 12 times higher during the first hours of the test. However, it is nevertheless pertinent to note that within several days after tests in sea water, a large crack appears at the coating – substrate interphase at the end of the sample. It is conceivable that sea water finds its way into the pores and erodes the substrate surface.

Figure 12 shows the microhardness of the coating and the surface layer of the sample as a function of depth. One can see that the microhardness value on the coating surface is slightly lower than inside the coating, where it is approximately 2.5 times higher than in the surface substrate layer. The transition region (the regions of the coating – substrate junction and the near-surface layer) have increased microhardness over a depth of almost 100 μm from the junction surface.

The X-ray structural investigation conducted showed that the main component of the surface layer of the coating produced by the pulsed plasma technique from the Hastelloy powder is nickel with the lattice constant $a = 3.6251$ Å. The lattice constant is increased in comparison with tabular data [38, 61], the relative microdeformation of the lattice $\Delta a/a_0 > 0$ and is equal to 2.8%. The increase in the lattice constant testifies to a crystal lattice distortion of nickel, which was subjected to pulsed plasma processing, due to microstress induced by the main components of the source powder (Mo, Cr, Fe, W) dissolved in it (Ni). Also observed in the coating are traces of chromium and the solid-dissolved N-phase Fe-Cr-Mo [38]. In addition, carbide and oxide phases are present in small amounts in the coating: W_2C, $Mo_{2r}C$, FeO, and Fe_3O_4. Hexagonal tungsten carbide and hexagonal molybdenum carbide with the lattice constants $a(Mo_2C) = 2.951$ Å, $a(W_2C) = 2.951$ Å and $c(W_2C) = 4.663$ Å, $c_{tabl} = 4.633$ Å (which is practically consistent with the data in Ref. [61], $a(Mo_2C) = 3.00$ Å, $a(W_2C) = 2.99$ Å and $c(W_2C) = 4.72$ Å, $c_{tabl} = 4.71$ Å) have mosaic blocks estimated at about 15 nm from the dimensions of coherent scattering domains. An estimate of coherent scattering domains of the main phase shows that the dimensions of crystallites in the surface layer of the coating range from 12 to 30 nm.

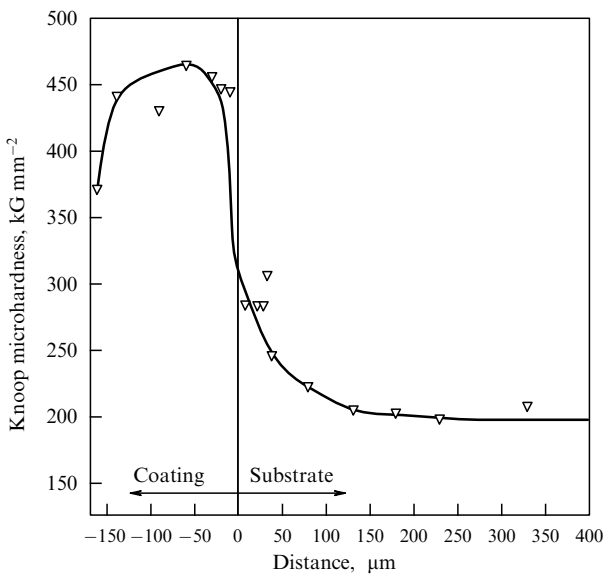

Figure 12. Variation of microhardness measured with a Knoop pyramidion (100 G load along the depth of a Hastelloy coating and the near-surface layer of an SS-400 steel substrate).

On the basis of X-ray phase analysis (XPA) data, it may be inferred that the surface layer of the coating is a multiphase nanodispersed structure that consists of the Ni-Cr-Fe nickel-based solid solution with an insignificant amount of the Fe-Cr-Mo iron-based solid solution, a mixture of oxide phases (Mo_2C, FeO, and Fe_3O_4), and traces of the initial powder components. All this is entirely consistent with the data obtained using transmission electron microscopy.

Therefore, the authors of Ref. [61] arrive at the following conclusion: the nickel-based Hastelloy coating deposited on a low-carbon steel substrate consists of ferrite polycrystals (grains), with a cellular dislocation structure observed inside the grains. Located along the subgrain boundaries are second phase precipitates — molybdenum carbide $MoC_{0.54}$. On the surface of the coating, a nanocrystalline layer of oxycarbide phases with crystallite dimensions $\sim 20 - 30$ nm forms. Located on the surface itself is a nanocrystalline oxide film of Fe_3O_4. No oxide layer was discovered in the coating – steel contact zone. The carbon-saturated layer amounts to 1 μm in thickness and the oxygen-saturated layer to 1.7 μm. Corrosion tests performed in sea water showed an almost three-fold reduction of corrosion potential and a nearly 12-fold rise in corrosion resistance. However, a corrosion crack is formed between the coating and the substrate within three days following the commencement of the test.

4. Ceramic and ceramic-metal coatings deposited on a metal substrate

4.1 Phase and elemental composition of aluminum oxide and its properties

We consider one more area for harnessing high-speed plasma jets. In Refs [37, 41], the structure of Al_2O_3 coatings deposited on a steel-3 substrate was investigated.

The elemental analysis of the pulsed-plasma coating of aluminum oxide was performed using Rutherford backscattering and elastic resonance with protons. Figure 13a shows the energy spectrum of elastic resonance with protons for a sample of the resultant coating. The spectra clearly show the presence of oxygen, aluminum, and iron, as well as a significant content of carbon in the surface layer of the coating. The structural formula of the coating formed by pulsed-plasma deposition can be expressed as $Al_{38}O_{59}Fe_3$. The carbon density in the surface layer of the coating amounted to 20 at. %. The emergence of iron in the oxide

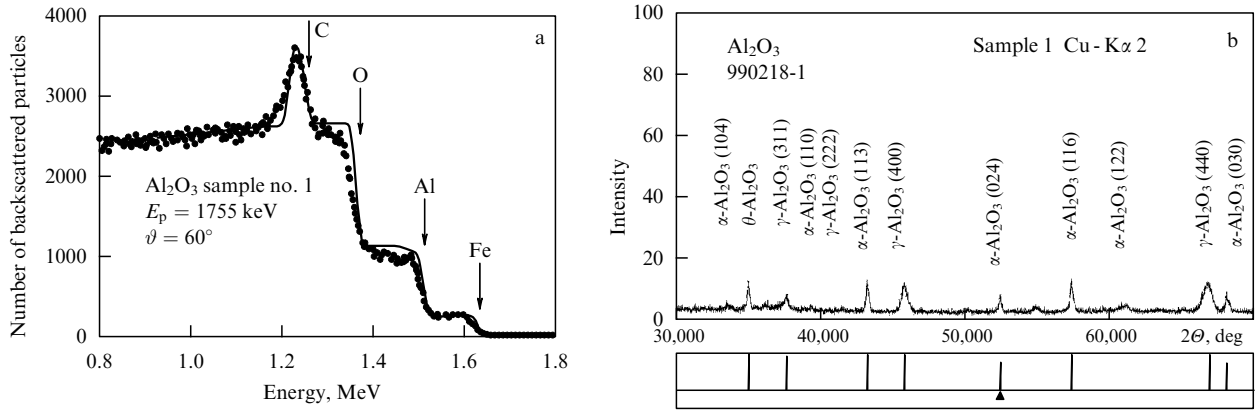

Figure 13. Energy spectrum obtained by the method of elastic resonance with protons (a) and X-ray diffraction pattern (b) of the plasma-detonation Al_2O_3 coating (the distance to the nozzle is 40 mm).

coating is due to the erosion of a steel electrode in the plasmatron combustion chamber during plasma jet production [41 – 43].

A local phase and structural analysis performed with the aid of transmission electron microscopy (TEM) with microdiffraction showed that the coating under investigation has a multiphase polycrystalline structure and consists of α-Al_2O_3, β-Al_2O_3, γ-Al_2O_3, and δ-Al_2O_3. The α-Al_2O_3 crystallites measure about 0.25 μm, have a regular faceting, and are free from defects. The other phases (β-Al_2O_3, γ-Al_2O_3, and δ-Al_2O_3) are crystals with dimensions of 0.1 – 0.3 μm, with a defect substructure in the form of separate dislocations observed inside them. The coating domains adjacent to the substrate contain a transition layer made of an AlF intermetallide with crystals measuring 20 – 40 nm. On the whole, this layer exhibits a high dislocation density caused by the shock action of the plasma-detonation wave.

X-ray structural analysis, which yields integral information about a layer several micrometers thick, also showed the presence of α- and γ-phases of Al_2O_3, the calculated phase ratio turning out to be as follows: α-Al_2O_3 — 30%, γ-Al_2O_3 — about 60%, the remaining — β- and δ-phases (Fig. 13b).

An analysis of the effect of phase composition on the physicochemical and mechanical characteristics of the pulsed-plasma coating of aluminum oxide suggests that the increase in content of the stable γ-phase, as well as of other (metastable) phases, lowers the hardness, wear resistance, and corrosion resistance of the coating. However, the coating – base adhesion is improved and the density of the coating itself increases. At the same time, it has been known [44, 45] that the polymorphous transformation $\gamma \leftrightarrow \alpha$ in Al_2O_3 on heating in the 1050 – 1300 °C temperature interval is attended with a significant change of volume. This may result in coating cracking and its exfoliation from the substrate when the γ-phase exceeds 80% in the two-phase coating or the coating is thicker than 0.3 mm. In the present instance, as shown by the authors of Refs [44, 45], the presence of several phases produces a relaxing stress gradient, which hinders the formation of cracks in the coating. The average density of the coatings produced by the pulsed-plasma technique was equal to 3.90 g cm^{-3}; this is slightly lower than the density of α-Al_2O_3, which is equal to 3.98 g cm^{-3} according to the data in Refs [46, 47]. At the same time, the highest hardness of the coating produced by the pulsed-plasma technique amounted to 1.98 GPa and the thermal conductivity coefficient to 38 W $(Mk)^{-1}$, which is close to the corresponding values for α-Al_2O_3 [46, 47].

Therefore, the use of pulsed plasma technology for Al_2O_3 coating deposition makes it possible to produce dense multiphase coatings that have a good adhesion with the substrate (due to the damping properties of the stable low-temperature γ-phase and the metastable β- and δ-phase modifications) and excellent physico-mechanical properties (due to the high content of the α-phase).

4.2 The hard WC-Co alloy

An example of the use of pulsed plasma jets to deposit a coating of a hard alloy (WC-Co metal ceramics) on a Cu substrate is provided in Refs [62, 63].

In a surface layer up to 2.8 μm in thickness, the content of Co, W, C, and O is in the following ascending sequence: WC_{89}; Co_8; C_2; O_2. Attention is drawn to the fact that the tungsten density on the surface of the coating is very low (about 1 at. %) and the carbon density amounts to 30 at. %. As is known from Refs [33, 32, 64, 65], in the deposition of tungsten carbide by a high-velocity oxygen fuel (HVOF) spraying and a high-energy plasma (HEP) jet, the respective percentage of tungsten in the coating is as high as 84.38% and 87.98%. Even a partial amorphization of complex phases located at the carbide and cobalt grain boundaries is possible [32]. The content of cobalt also changed, to 12.98% (HVOF) and 9.22% (HEP). The carbon density changed from 4.09% in the initial powder to 2.5% (HVOF) and 2.52% (HEP). In Ref. [32], the basis of the coating is constituted by phases, the majority of which were present in the initial powder, but there also appeared other phases produced due to high-rate hardening.

A phase analysis carried out using a Dron-3 facility (K_α-Cu) demonstrates that the main phase of the coating is WC with a face-centered close-packed (FCP) lattice. The authors made judgements about the presence of other phases from reflexes in the temperature interval from 27 to 87 °C (Fig. 14). In this interval, several lines overlap, which hinders the phase analysis. The interplanar spacings calculated from the reflexes that were possible to extract suggest that the following phases were present in the coating: W_2C, Co_7W_6, Co_3W, W, and Co. Complex phases in the intercrystallite space may be in an amorphous state, which is consistent with the data in Refs [62, 63]. This state is attributable to the high-temperature cycle in the production of the coating.

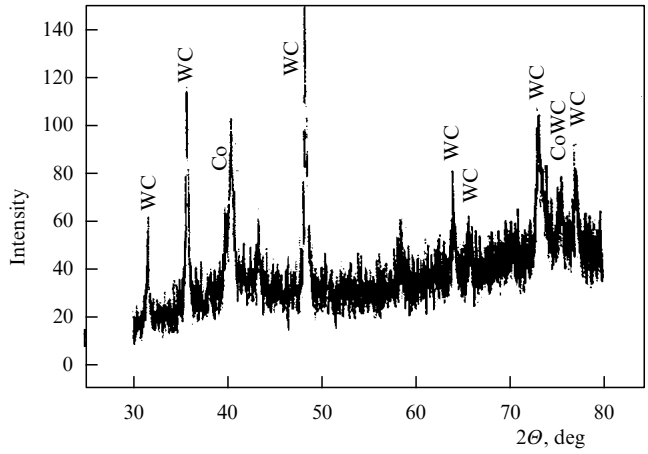

Figure 14. Part of the X-ray diffraction pattern recorded for a WC-Co coating.

The structural phase analysis of the metal ceramic WC-Co coating performed with the aid of transmission electron microscopy (TEM) with diffraction showed that the coating has a polycrystalline structure represented by WC crystallites with a hexagonal lattice, the crystallites α- and β-Co and WC with a cubic lattice (Fig. 15). The average size of WC crystals with an FCP lattice is equal to 0.15 μm and of cobalt crystals to about 25 nm. Co_3W_3C phase particles measuring about 15 nm are observed along the crystallite boundaries [66]. The WC crystallites with a cubic lattice have

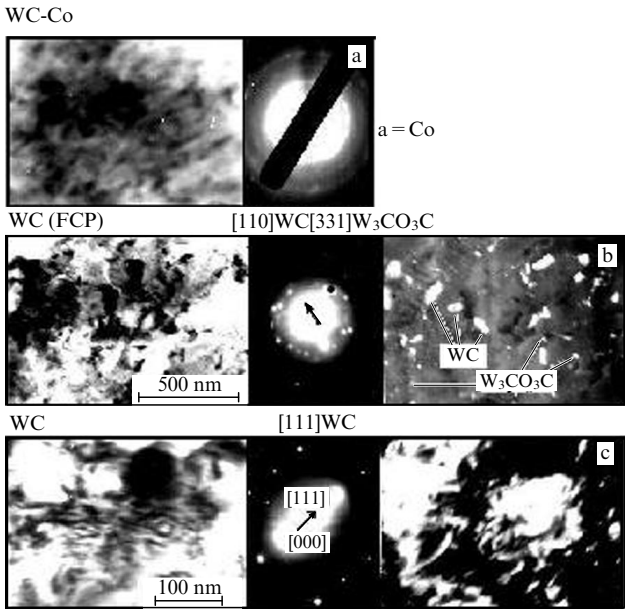

Figure 15. Electron microscope WC-Co coating images obtained with a TEM with diffraction: (a) morphology of cobalt polycrystals with the average dimension about 25 nm, diffraction by local regions with Co polycrystals; (b) morphology of tungsten carbide (WC) regions, face-centered close-packed lattice, average crystallite dimensions 0.15 μm, nanoparticles of the W_3Co_3C phase with the average size ~ 15 nm are observed along the grain boundaries, diffraction from local regions of carbide WC and W_3Co_3C; (c) morphology of regions with cubic-lattice tungsten carbide (WC), a dislocation structure substructure is observed inside the crystallites, dark- and light-background images, diffraction by local regions of the coating in the presence of cubic WC.

an internal dislocation structure. According to measurement data, the microhardness of the WC-Co coating on the surface and on an oblique metallographic section ranges from 10^4 to 1.5×10^4 N m^{-2} and the coating – substrate adhesion strength ranges from 210 to 280 MPa for different parts.

4.3 Structure and morphology of the coating of the hard Cr_3C_2-Ni alloy

In Ref. [67], the Cr_3C_2-Ni alloy coating deposited on a copper substrate was investigated.

An analysis of coating diffraction patterns measured on a Dron-2 facility with cobalt radiation showed that the coating comprises a single phase — Ni-based solid solution with the lattice constant $a = 3.525$ Å (the tabular datum for Ni is $a = 3.524$ Å). Also formed is the Cr_7C_3 compound, but this phase is more weakly pronounced and metallic Cr belongs to the intermetallide Cr_3Ni_2.

Figure 16 shows images of the coating surface (a) and a fracture of the coating (b). The coating structure and morphology significantly vary with depth: there are bright parts (typical of chromium carbide) and glittering dark parts (typical of the metallic phase of nickel). A microanalysis of these regions revealed the presence of Cr, Ni, O, Cu, and Fe in the coating, with glittering parts containing only Ni with a small admixture of Cr and Cu. The parts with a glittering appearance were found to contain about 96% Ni and about 4% Cr. In this region, clearly, there is a grain or a powder particle of nickel with a low content of Cr, which appeared as a result of particle fusion and mixing in the liquid phase or gaseous plasma state during the flight of the powder particles of Cr oxide and metallic Ni in the plasma jet. In domains with a gray background, the atomic density of Cr is equal to about 61%, of Ni to about 8.5%, of oxygen to about 5.6%, of copper to about 13.3%, of iron to 2.6%, and of aluminum to more than 5%, while the elements sulfur, calcium, and silicon account for less than 1%. It is believed that Cu penetrates from the substrate as a result of dynamic and temperature action of the plasma jet. The lattice constant of Cu is close to 3.614 Å, as is that of the Cr_3Ni_2 intermetallide, and the authors interpret this phase as intermetallic.

Coating hardness measurements from a transverse metallographic section carried out with the aid of a Rockwell pyramidion showed that the highest hardness value in the light part (Cr_7C_3 — the main phase) is equal to 66 ± 4.5 HRC and in the glittering dark parts with a predominance of a solid Ni solution to about 45 ± 1.5 HRC. Measurements of the coating – substrate adhesion strength performed by scraping a diamond pyramidion against a transverse and oblique section yielded values strongly different from those given, in the range between 25 and 300 MPa.

An analysis of surface hardness measurement data for different loads on the pyramidion (Table 5) allows concluding that the depth to which the pyramidion is forced is the same as the characteristic imprint dimension and is equal to dozens of micrometers. Considering the values of hardness in relation to the imposed load, we can draw the conclusion that the crystal (grain) dimension in the coating is of the same order of magnitude.

Figure 17 shows the variation of hardness with depth (an oblique section) measured for the same load on the pyramidion for a coating produced with a plasma-detonation facility. The measurements were made only on gray parts of the coating to ensure more trustworthy information about the variation of hardness with depth in the coating.

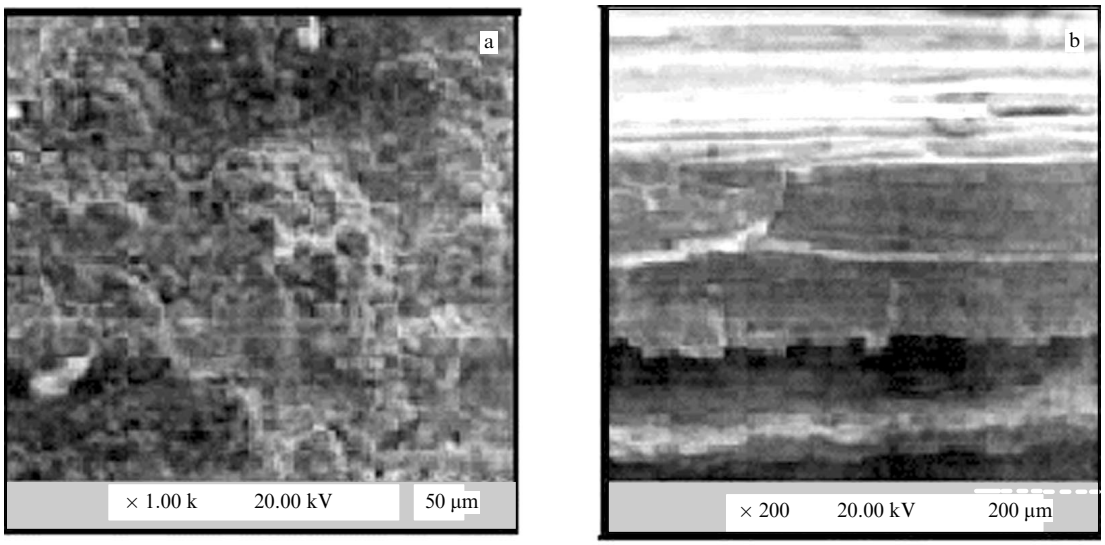

Figure 16. (a) Surface morphology of a Cr_3C_2 coating (30 at. % of Ni) determined with the aid of a scanning electron microscope. (b) Cr_3C_2 coating (30 at. % of Ni) structure in the region of a transversely cleaved coating.

Table 5. Rockwell hardness measurement data for the coating surface for different loads on the pyramid.

Test series no.	Load, G	Hardness, HRC	Note
1–4	50	58 ± 1	Gray background
	100	51 ± 3	
	200	48 ± 5	
6, 8, 9, 12	50	62 ± 4	Uniform
	100	56 ± 1	gray background
	200	50 ± 1	
10, 11, 13	50	27 ± 7	Light background
	100	35 ± 3	
	200	50 ± 12	

As shown in Ref. [67], for optimal design conditions for depositing a coating of chromium carbide with 30 at. % of Ni, it is possible to attain a rather high coating quality, a high hardness (up to 66 HRC), and a good adhesion (up to 300 MPa). The coating then consists of a Ni-based solid solution, complex Cr carbides (Cr_7C_3), and an intermetallide Cr_3Ni_2; the formation of CrO is also possible. Tests of components of thermal power plants, like impeller blades and steam generator tube surfaces operating in an oxidizing medium (air) or in a slag environment (slag particles) at high temperatures (300–800 °C), with a Cr_3C_2-Ni coating deposited with a pulsed plasma jet demonstrated their durability and operability.

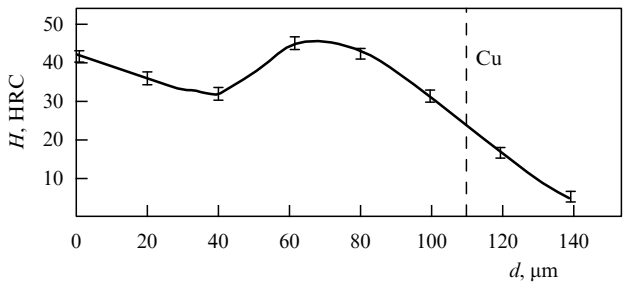

Figure 17. Hardness as a function of depth in a Cr_3C_2-Ni coating (oblique metallographic section) for a pyramidion load of 50 G.

4.4 Structure and properties of the powder coating of aluminum alloys (Al-Co, Al-Ni)

In Refs [68, 69], Al-Co and Al-Ni coatings deposited by a plasma-detonation technology on copper and aluminum alloy substrates were used.

Aluminum alloys combine an enormous wealth of merits: low density, high strength-to-weight ratio, high electric and thermal conductivities, good plasticity and viscosity, and high corrosion resistance to many organic acids and sea water. These properties make them indispensable in many branches of industry. Among the disadvantages of aluminum alloys are low hardness, a low elastic modulus, high chemical activity with many inorganic acids, and low wear strength. These drawbacks can be overcome by depositing a surface coating of other materials to increase hardness and improve corrosion resistance. Co and Al are known to form intermetallide phases, and it is therefore of interest to produce a coating that contains Al along with another element (Co) able to strongly modify its properties. Furthermore, the use of high-speed plasma jets to coat metallic substrates opens up broad possibilities for fabricating high-quality coatings of metals and alloys (different from the substrate in composition).

For a base in Refs [68, 69], Cu substrates and an Al-Mg-Mn alloy vere used. The latter is among aluminum alloys that are not amenable to strengthening by thermal processing [1]. A coating of an Al-Co powder was deposited on samples measuring 14 × 20 mm using a plasma-detonation 'Impul's-5' facility with the following parameters: pulse repetition rate from 2 to 4 Hz, capacitance $C = 550$ μF, sample–plasmatron nozzle distance $H = 550$ mm, translation velocity no higher than $V = 0.5$ cm s^{-1}, the number of passes 2–4, powder dimensions 35 ± 68 μm (a mixture of Al and Co).

Figure 18 shows the results of a surface layer analysis of the Al-Co coating deposited with a high-speed plasma jet; the analysis was performed by elastic scattering of protons (elastic recoil detection analysis, ERDA) [70]. As is seen from the spectra, in addition to Al and Co, the coating

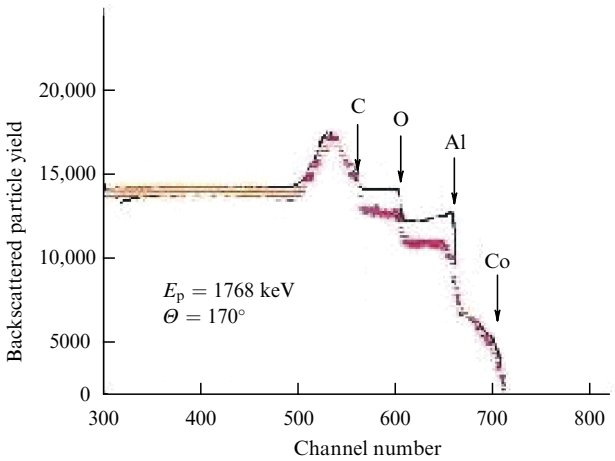

Figure 18. The energy spectrum obtained on an Al-Co coating measured by elastic recoil detection analysis (ERDA) on protons. The coating is deposited on a Cu substrate.

contains oxygen (at a high density, up to 19 – 17 at. %) and carbon (at a low density, from 2.5 to 1.5 at. %) in a layer up to 2.5 μm in depth. At the same time, oxygen is present in a layer almost 22 μm thick in the surface layer of the coating (Table 6). A SIMS analysis revealed the presence of N^+, Al^+, AlN^+, AlO^+, Al_2^+, AlN_2, AlO_2^+, Al_2N^+, CoN^+, and CoN^+. Because we intentionally gave no attention to nitrogen in the Rutherford backscattering analysis, it is safe to assume that along with oxygen, the surface layer contains nitrogen, which forms the AlN_2^+ and CoN^+ clusters during the plasma jet flight through the barrel and the barrel – material distance. Furthermore, there are various clusters (a wide variety) of Al oxides (AlO; AlO_2), which in aggregate produce the Al_2O_3 compound.

Table 6. Elemental composition of the Al – Co coating, at. %.

Coating depth, nm	Co	Al	O	C
83.7	6.43	72.79	19.11	1.67
248.5	8.53	71.04	18.39	2.04
437.8	10.68	68.99	18.00	2.33
714.1	11.42	68.09	17.84	2.65
1108.4	13.23	66.43	17.38	2.96
1497.0	14.79	64.67	16.88	3.66
1885.6	14.79	64.67	16.88	3.66
2276.9	14.91	65.31	16.98	2.80
5516.5	14.96	68.00	17.04	0.00
13,615.7	14.96	68.00	17.04	0.00
21,714.9	14.96	68.00	17.04	0.00
29,339.5	18.03	81.97	0	0.00

A morphology investigation of the coating over its surface and throughout its depth (an oblique metallographic section) showed that the typical structure that emerges under the dynamic action of a plasma jet and its temperature action [71, 72] forms on the surface. A significant roughness is observed, which corresponds to the characteristic size of Al and Co powder particles, or particles that become molten during the plasma jet flight. The coating hardness measured with a Vickers pyramidion was found to be significantly higher, by almost a factor of two, than the hardness of the coating itself. It is noteworthy that a rise in hardness was discovered in the transition layer. The adhesion strength determined by scraping a diamond pyramidion against a transverse metallographic section was in the range between 12.5 and 22 kg mm^{-2}. This is a rather strong adhesion.

From an analysis of X-ray diffraction patterns for the Al-Co coating surface, there follows the occurrence of three FCC lattices. An analysis of the resultant data revealed one α-Co lattice. Its constant is equal to 3.515 Å. A significant part of the diffraction pattern peaks belong to aluminum with the lattice constant 4.088 Å. The presence of Cu with the lattice constant 3.614 Å was revealed in the surface layer, which is due to evaporation of the copper electrode.

The diffraction pattern also shows numerous peaks that match to the compounds Al_2Co_{15}, Al_2Co_{19}, and Al_4Co_{113}. Considering that the aluminum solubility of cobalt is low (below 0.4 at. % in the liquid state and below 0.01 at. % in the solid state), the formation of cobalt – nickel intermetallides is quite possible.

Calculations yielded the following phase percentage in the coating: 71% Co, 13% Al, 6% Cu, 5% Cu_2Al_{15}, and 4.5% ($Co_2Al_{19} + Co_4Al_{113}$) (the last figure is given for the two compounds taken together, because many of their peaks fall into the same regions of the rise of the diffraction pattern background and are hardly possible to separate).

Therefore, it was shown that the use of a high-speed pulsed plasma jet for depositing an Al-Co coating on a copper alloy leads to an increase in microhardness (a two-fold increase relative to the substrate) and a strengthening of adhesion.

In Ref. [69], an investigation was made of Al-Ni coatings deposited on a Cu substrate. Because the properties of a material are largely dependent on the state of its surface, this work was concerned with surface coating morphology. Experimental data testify to the formation of a surface corresponding to a typical relief of a coating obtained in the powder deposition with a high-speed pulsed-plasma jet on a substrate. The thus produced coatings have a highly developed relief with extensive roughness. Observed on the surface is the alternation of silver-gray segments with inclusions of small gray bumps, which look like incompletely fused powder particles stuck together. With a higher magnification, it is possible to clearly see numerous depressions of indefinite shape on the surface. Bright glittering segments were recorded on the surface. According to microanalysis data, aluminum is the dominant element in these segments, its density in them being approximately one order of magnitude higher than the density of the main powder component, nickel. The integral characteristic of this segment suggests that the coating is primarily made up of Ni and Al. In addition, there are elements such as Fe, Cr, Cl, Ca, and Si on the surface. They may settle on the surface of the coating in the combustion chamber of the plasmatron. Ca is among the uncontrollable impurities, because it supposedly finds its way onto the coating surface when the samples are brought into the atmospheric air. The Ni-to-Al density ratio is varied over the surface (in dark and gray parts, the Ni density is substantially higher than the Al density). The resultant microanalysis data allow concluding that Ni is the predominant element of the surface (up to 1 μm in thickness).

The surfaces were additionally analyzed using Rutherford backscattering and ERDA. From the energy spectra of the elastic resonance of nuclear reactions (with the initial α-particle energy 1768 keV) and proton backscattering (with the initial proton energy 2020 keV), it is clear that the thin surface layer of the coating contains the main constituents of

the initial powder, aluminum and nickel. High densities of carbon and oxygen were recorded in the coating. The existence of a shelf in the spectrum and the disagreement of the calculated data as well as of experimental data are indicative of the formation of nickel – aluminum intermetallide compounds at the surface (close to Ni_4Al in stoichiometry). Conceivably, the coating contains the Ni_3Al compound and pure Ni, which gives the above stoichiometry in the aggregate. The effective profiles of all elements were calculated and the density distribution of constituent elements with depth were determined from the spectra obtained. Judging by the data, the coating surface is strongly saturated with oxygen and carbon, their density beginning to lower rapidly with greater depth in the material (to 1 μm). A low nickel density was recorded at the coating surface (7.2% for $h = 37$ nm), but its density strongly increases with the approach to the substrate (up to 65%) and it becomes the main component of the coating matrix. The authors attribute the high surface aluminum density to the fact that aluminum is the lighter fraction with a low melting temperature and is primarily in the molten state in the plasma jet. When the plasma jet interacts with the surface, dynamic action and deformation of Ni powder particles occur, and the molten gas – plasma phase of Al completes the surface coating.

According to the results of investigations conducted, the source PT-NA-001 powder consists of 93.5% nickel and 6.5% aluminum. The respective lattice constants of the coating constituents are a (Ni) = 3.524 Å (a_{tab} (Ni) = 3.5238 Å [73]) and a (Al) = 4.054 Å (a_{tab} (Al) = 4.0484 Å [73]). The coating is accompanied with several phase transformations in the source powder material. By analyzing the fragments of the X-ray diffraction patterns of powder composition in the initial state and in the resultant coating, it was determined that the coating surface consists primarily of Ni atoms (85%). Along with the main phase of the powder matrix, phases such as NiO (4%) and Ni_3C (3%) are formed in the coating. The selected coating regimes favor the formation of intermetallide nickel – aluminum compounds in the coating. We determined that the coating surface is comprised of about 5% Ni_3Al. The X-ray diffraction pattern also clearly shows the presence of a small amount of pure aluminum on the surface (up to 3% in density).

The coating – substrate adhesion strength varies significantly from segment to segment. In the tests conducted, the adhesion strength ranged between 28 ± 2.2 and 45 ± 3 MPa.

The microhardness values in the measurements over the surface and the transverse section of the coating showed a significant scatter. In the coating segments under investigation, they ranged from 65 ± 3.5 to $3.0 \times 10^2 - 4.2 \times 10^2$ kG mm^{-2}. The authors believe that the surface microhardness peaks in the segments where nickel – aluminum intermetallide compounds and nickel carbide prevail in density, whereas lower values of the characteristic involved can be observed in segments with a prevalence of pure nickel or aluminum, as well as small additions of iron and chromium, which find their way onto the coating surface from the eroding electrode of the plasmatron.

Thus, it was determined in Ref. [69] that the coating deposition of nickel and aluminum powders using pulsed plasma spraying is attended with phase transitions in the source powder and production of intermetallide compounds. The components are redistributed due to fusion of the source material in the plasma flow, with the consequential emergence of local segments on the coating surface with a high aluminum density (up to 83%). The coating saturation with the gases of the plasmatron atmosphere underlies the production of an oxide film and nickel carbide on the surface. Partial fusion of the source powder results in the production of the Ni_3Al intermetallide compound. Most likely, precisely the presence of the carbide and nickel intermetallide on the surface is responsible for local surface strengthening.

5. Characteristics of the structure and physico-mechanical properties of hybrid and combined coatings

5.1 Structure and properties of hybrid Al_2O_3/Cr/TiN coatings deposited on a steel-3 substrate

Of special interest are protective coatings for components of electrochemical and chemical equipment. It is well known that individual kinds of processing, e.g., ion implantation, ion-assisted thin-film deposition, electron-beam processing, and coating with high-velocity plasma jets [70, 74 – 81] cannot furnish the desired result. That is why combined processing techniques are currently employed to solve applied problems, making it possible to solve important problems in material science [82]. At the same time, it is well known that components such as, e.g., acid pump blades require a strong adhesion of the coating to the component surface, a low porosity, and the presence of passivating elements like Cr, Ti, etc. [83, 84].

In Ref. [83], investigations were made of the structure and the elemental and phase composition of an Al_2O_3/Cr/TiN-based coating, which was deposited on a steel-3 (0.3 mass% of C) substrate, prior to and after electron-beam irradiation, as well as of the service characteristics of the hybrid coating. Particular emphasis was placed on diffusion and mass transfer.

Protective coatings were obtained on thin samples (0.3 mm thick) of austenitic stainless steel-321 (composition: 18 mass % Cr, 9 mass % Ni, 1 mass % Ti, and the balance Fe). The deposition technique of protective hybrid coatings was as follows. A high-speed pulsed plasma jet of the 'Impul's-5' facility was employed to deposit the base powder coating of aluminum oxide (α-Al_2O_3 powder with powder particles measuring 27 – 56 μm) of thickness 45 – 65 μm for the following operational characteristics of the facility: the detonation frequency (pulse repetition rate) 4 Hz; the electric energy consumption per plasma pulse $(2.5 - 3.5) \times 10^3$ J; the distance between the nozzle exit section of the plasmatron and the substrate 40 cm; the spot diameter 33 mm. To improve the corrosion properties of the surface in sulfuric acid, a layer of titanium nitride (TiN) of thickness 1.2 – 2 mm was deposited on the Al_2O_3 coating in a vacuum-arc source of the 'Bulat-3T' type. Prior to the deposition of the titanium nitride layer, the ceramic surface was coated with a Cr sublayer (0.2 – 0.5 μm thick) to strengthen adhesion.

Upon deposition of the hybrid coating, part of the samples were set aside for investigations in the initial state and part of them were used for further modification [83].

The surface of the hybrid coating was exposed to a high-current electron beam (HEB). The e-beam energy density was selected in such a way as to completely fuse the Al_2O_3/Cr/TiN coating and to partly fuse the substrate.

The photographs of the surface layer of the Al_2O_3/Cr/TiN coating prior to and after HEB irradiation show that the surface has a large roughness (Fig. 19). An analysis of

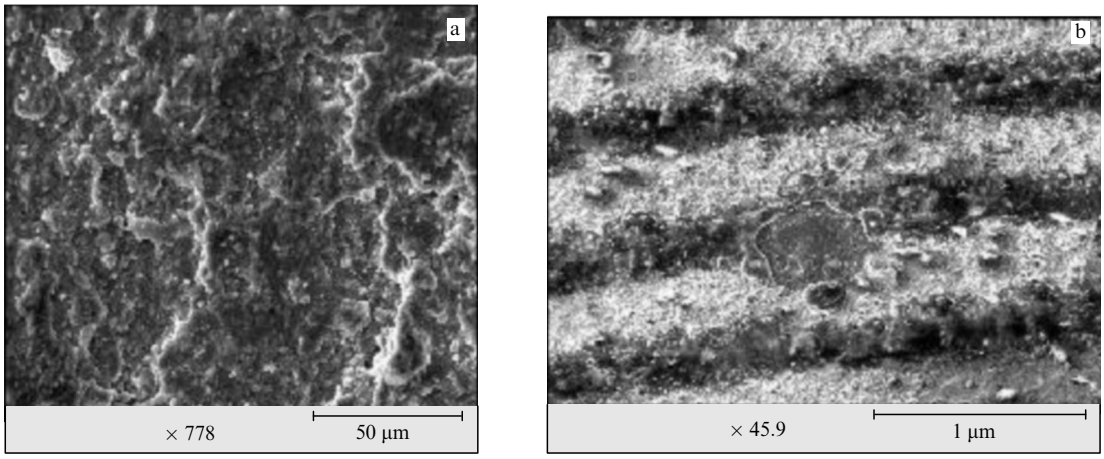

Figure 19. Surface structure of hybrid coatings deposited by a combined technique: (a) Al_2O_3 coating without fusion in the absence of an HEB, (b) HEB-irradiated Al_2O_3/Cr/TiN coating after fusion.

investigation data also testifies to a large roughness, because the vacuum-deposited Cr and TiN films replicate the relief of the coating deposited with a pulsed-plasma jet. It is noteworthy that the formation of the 'droplet' fraction, which is seen on the surface of the hybrid coating, is due to the segregationless deposition of TiN and Cr. HEB irradiation of the hybrid coatings results in the formation of a 'striate' surface structure [alternation of bright (the initial state of the coating) and dark streaks (the surface fused by the electron beam)]. The spots in these streaks that were subjected to microanalysis are marked with points.

Figure 20 shows the spectra recorded from different regions of the coating surface. For rounded inclusions ('droplet' fraction regions), the spectra of the elements Ti, Cr, and Fe (see Fig. 19) were obtained. Titanium is the predominant element. The densities of the above elements were found to vary from point to point. The presence of Al was additionally discovered. The regions not subjected to HEB irradiation contain 13.9 mass % Al, 48.2 mass % Ti, 0.03 mass % Cr, and 0.42 mass % Fe. The regions fused by the HEB contain about 55 mass % Al, 0.5 mass % Ti, 0.2 mass % Cr, and 0.8 mass % Fe.

The elemental composition of hybrid coatings was investigated in greater detail using backscattered protons. The spectrum identification is given in Fig. 20b (the presence of Al, Ti, oxygen, and nitrogen on the surface of the hybrid coating upon HEB irradiation). The backscattering analysis testifies to an increase in oxygen density in the coating (up to the very surface) in the samples exposed to the HEB. In the near-surface layers of the coating without HEB, the oxygen density is substantially lower. According to the data obtained, the coatings exposed to the HEB exhibit a lowering of the Ti content with depth and simultaneously a broadening of its distribution profile. Proceeding from the diffusion theory and considering the good agreement between the form of the Ti density distribution and the Gaussian curve, it has been possible to calculate the effective diffusion coefficient for titanium (2.4×10^{-8} cm^2 s^{-1}) [85–87].

Using the same samples, the authors of Ref. [88] investigated the phase composition (XRD analysis) of the hybrid Al_2O_3/Cr/TiN coatings. The resultant data indicate that the main element of the substrate matrix is γ-Fe (FCC) with the lattice constant 3.592 Å. According to the XRD analysis, which provides an integral characteristic of a layer several micrometers thick, the hybrid coating is a multiphase compound. Present along with the main phase of the powder α-Al_2O_3 are γ-Al_2O_3, β-Al_2O_3, TiN, and Cr. The phase percentage was estimated for the coatings subjected to two

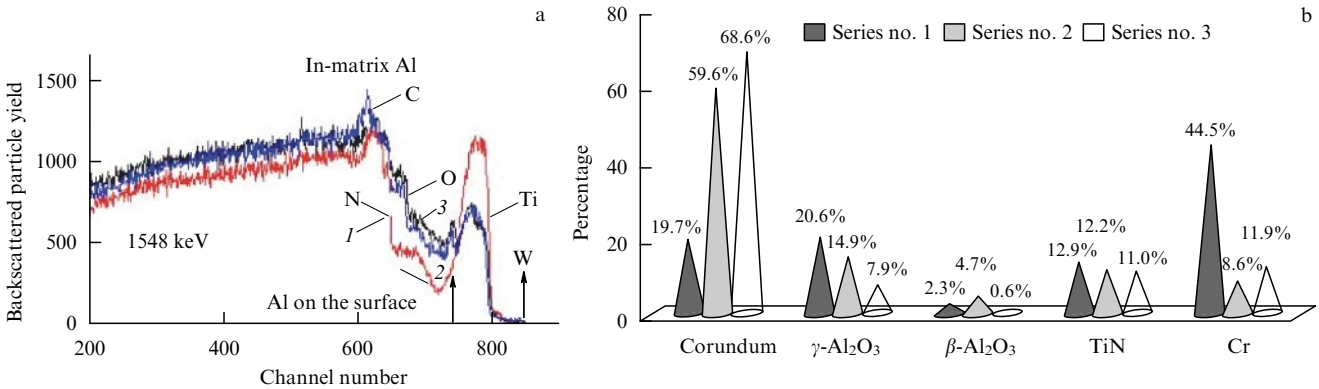

Figure 20. (a) Energy spectrum of backscattered protons with the initial energy 1548 keV: *1* — initial coating, *2* — coating exposed to the HEB with a lower energy density, *3* — coating exposed to the HEB with a higher energy density, (b) calculated phase percentage of hybrid coatings derived from X-ray diffraction patterns.

processing regimes (series no. 2, series no. 3). The calculated data are given in Fig. 20b. One can see that the HEB-induced modification of the Al_2O_3/Cr/TiN coating leads to the polymorphous transformations $\gamma \rightarrow \alpha$ and $\beta \rightarrow \alpha$ in Al_2O_3. This allows concluding that the HEB-induced modification of the surface has a significant effect on the lattice parameters of the constituent coating elements.

Changes in the α-Al_2O_3 lattice parameters were discovered, which were related to the formation of residual compressive stress [series no. 1 (without HEB irradiation): a (α-Al_2O_3) = 4.773 Å, c (α-Al_2O_3) = 13.581 Å, $c/a = 2.87$; series no. 2 (HEB irradiation with the lower power density): a (α-Al_2O_3) = 4.773 Å; c (α-Al_2O_3) = 12.996 Å; $c/a = 2.72$; series no. 3 (HEB irradiation with the higher power density): a (α-Al_2O_3) = 4.767 Å; c (α-Al_2O_3) = 12.878 Å; $c/a = 2.71$] [85, 73].

In the initial state, prior to HEB irradiation, for instance, the lattice constant of titanium nitride is equal to 4.264 Å, while it is equal to 4.221 Å upon HEB irradiation (the regime of partial fusion). Upon HEB processing with complete fusion of the combined coating, the lattice constant becomes equal to 4.247 Å. The Cr lattice parameter was found to change [series no. 1: a (Cr) = 2.879 Å, series no. 2 and no. 3: a (Cr) = 2.868 Å].

Additional investigations were undertaken to gain a more exact interpretation of the data on the elemental coating composition by Auger-electron spectroscopy [83]. When an atom is in a bound state, the energy of Auger electrons is somewhat different from the initial state of the element and additional peaks appear in the spectrum [88]. An analysis of elemental density profiles with depth of the hybrid coating yielded an estimate of its thickness, which is equal to 2.5–3 μm with Ar^+ ion etching for 30 min. It is pertinent to note that a broad spectrum of elements and their compositions (compounds or clusters) was discovered in the coating. A high density of Ti and N is observed near the surface; then, upon increasing the etching time, there emerge Cr and Al peaks, as well as Cr_2 and Cr_2Fe_3 clusters.

Table 7 gives some data of corrosion tests. The lowering of corrosion potential E, like the lowering of corrosion i_{cor} and passivation i_{pas} currents in the case of electron action on the Al_2O_3/Cr/TiN coating, testifies to a good corrosion resistance of the hybrid coating to sulfuric acid. It is believed that this improvement in corrosion resistance is related to a decrease in through pores in Al_2O_3 with an increase in coating thickness, which is due to TiN and Cr and its mixing with the ceramic layer [86].

Table 7. Results of corrosion tests of Al_2O_3/Cr/TiN coatings on AISI 321 type stainless steel in a solution of sulfuric acid with a molar concentration of 0.5M.

Test series number	Sample	E, mV	i_{cor}, mA	i_{pas}, mA	E_{pas}, mV	E as mV
1	Al_2O_3 + TiN Initial state	– 425	3.8	1.15	1015	1012
2	Al_2O_3 + TiN Partial HEB-induced surface fusion	– 360	0.15	0.14	970	935
3	Al_2O_3 + TiN Complete surface fusion with a partial substrate fusion	– 265	0.95	0.5	985	970

It is also noteworthy that the density of the Al_2O_3 coating in the initial state is equal to 3.9 g cm^{-3}, while it is known from the literature that α-Al_2O_3 has the density 3.98 g cm^{-3}, and the Al_2O_3 coating adhesion to the substrate (without e-beam processing) is equal to 40–65 MPa [7]. However, the HEB processing of the surface with its complete fusion results in a significant strengthening of adhesion up to 140–160 MPa (which is also related to the fusion and mixing in the 'liquid' phase) [87].

The coating hardness without electron irradiation ranged between 1.3×10^4 and 1.42×10^4 N mm^{-2}; after irradiation in the soft regime (series no. 2), it was equal to $\sim 1.6 \times 10^4$ N mm^{-2}, and after irradiation in the hard regime (series no. 3) to $(1.78 \pm 0.8) \times 10^4$ N mm^{-2}. Therefore, one can see that the HEB processing increases the microhardness.

The deposition of Al_2O_3/Cr/TiN hybrid coatings with subsequent HEB processing in two regimes results in the variation of the phase composition of the coating (results of the XRD analysis), elemental (in particular, Ti) mass transfer (AES, BS, and microanalysis data), as well as a significant change in operational characteristics like adhesion, hardness, and corrosion resistance in sulfuric acid.

5.2 Physico-mechanical properties and structure of nickel-alloy coatings prior to and after electron-beam irradiation

Among the present-day techniques of producing corrosion-resistant materials with excellent operational characteristics, mention should be made of combined (duplex, triplex) methods of surface processing [15, 16]. Recently, a high-speed pulsed-plasma jet was used to deposit coatings of powder materials [82–86, 89]. However, these coatings have several drawbacks: the formation of thin oxide layers on the surface and the existence of pores in the coating (from 0.5% to 1.8%). To eliminate these disadvantages and improve adhesion in the coating–substrate region, advantage is taken of the combined processing of coating surfaces by pulsed plasma flows and electron beams with a high energy density [73]. Suchlike action of concentrated energy fluxes on the surface of a solid leads to absorption of a part of the energy, which is in turn responsible for the occurrence of diverse physicochemical effects in the surface material layer and in the depth of the coating (heating, structural phase transitions with a change of the aggregate state, change of the phase composition of the surface, plasma-chemical reactions, intensification of almost all diffusion mechanisms, etc.) [73].

Nickel-based alloys are known to be one of the main classes of powder materials for the production of corrosion-resistant coatings. Plasma coatings of nickel alloys are widely used to protect surfaces from corrosion and wear [90, 91].

Therefore, in Ref. [73], the authors solved the problem of obtaining Ni-based powder coatings on a low-carbon substrate by way of the plasma-detonation technique with subsequent fusion of the surface and a part of the substrate with a high-current electron beam. They also investigated the structure, phase composition, microhardness, hardness, and corrosion resistance of the resultant coatings.

To obtain wear- and corrosion-resistant hard coatings, the following research was undertaken in Refs [73, 90, 91]. Powder coatings of a nickel alloy (with the thickness between 60 and 110 μm) were deposited on low-carbon steel employing the 'Impul's-5' facility. Two kinds of powder (standard, Russia) served as the material for producing corrosion-resistant coatings with high operational characteristics: PG-10N-01 (Ni base, B — 3.3%, C — 0.8%, Si – 4.3%,

Cr — 14–20%, Fe — up to 7%) and PGAN-33 (Ni base, Cr — 24%, Mo — 4%, Si — 2%, W — 1%, B — 2%). It is pertinent to note that the additions of Si and B were introduced into the powder surface to reduce the forces of surface tension of the molten coating during its modification by concentrated energy sources. Mo and W are the alloying elements that increase the hardness of the resultant coatings.

Part of the samples under investigation were left in the initial state and part were fused with an HEB provided by a U-212 source. The HEB surface processing was performed in two regimes: soft (coating fusion) and hard (complete fusion of the coating and fusion of the substrate surface layer two times thicker than the coating itself), with the respective beam power densities equal to 1000 and 2000 W cm^{-2}. In this case, the e-beam translation velocity was equal to 80 m s^{-1} and the processed track width to 10–12 mm. It is noteworthy that the surface tension of the material depends strongly on the amount of energy incident on a unit surface area, which is due to the HEB-induced coating surface modification attended by high rates of heat removal inside the material surface [91, 92].

Microhardness measurements were carried out with a PMT-3 instrument with a diamond Vickers pyramidion for indenter loads of 20, 50, and 100 G. Measurements were made on transverse sections, inward from the coating surface [14].

Wear resistance tests were carried out on an SMTs-2 facility in a plane–cylinder configuration in the medium of technical Vaseline [73, 93], both on the base material and on coating surfaces [93].

The corrosion resistance of the modified coating was investigated with the aid of electrochemical equipment. The scanning velocity of the material surface (see Ref. [87]) was equal to 15 mV s^{-1}. The structure and the phase composition were analyzed in Refs [87, 73]. The surface microstructure research data are indicative of different surface morphologies of the coatings formed under the action of a pulsed plasma jet (with fused and molten powder) and the electron beam.

A study of surface images made with different magnification after pulsed plasma processing allowed the following conclusions. The microrelief appearance of the surface modified by the pulsed plasma jet testifies to the presence of a very large roughness (Fig. 21). Incomplete fusion of some powder particles in the pulsed plasma flow and their subsequent high-rate deformation on the substrate surface are responsible for the formation of the surface in the form of a clinker.

At some spots, it is possible to discern the outlines of solidified deformed particles. Clearly seen on the surface are separate, even dark segments of the coating, which obviously have a granular structure. In addition, one can see dents with a strongly pronounced relief of the bottom and alternating dark and light segments.

An analysis of the spectrum recorded from different spots on the surface of the coating upon pulsed-plasma fusion allows concluding that its main components are Ni (52 mass %), Fe (9 mass %), Cr (12.5 mass %), and Mo (21 mass %). Also detected were low concentrations (below 10 mass %) of Al, Si, and Ti. Local elemental analysis suggests an idea of a nonuniform redistribution of the elements that are components of the source powder and of the gas atmosphere of the plasmatron. The authors discovered regions wherein the highest Ni density was equal to about 75% and the lowest to about 3%. In this case, the density of molybdenum in the segments with the lowest nickel density ranged up to 84%. Considering that molybdenum is a constituent element of the PGAN-33 powder and that an eroding molybdenum electrode is employed in the coating, we believe that this local increase in density of the element is quite possible.

Investigations of the phase composition of the initial powder showed that it is an FCC structure similar to the solid solution of nickel substituted for chromium atoms. After pulsed plasma processing, the powder coating is a multiphase compound. From the calculated data and from fragments of the X-ray diffraction pattern recorded from the powder coating surface, it is evident that the base of the matrix is made of Ni (48%) and Mo (20%). The calculation also suggests that the Ni lattice undergoes some changes. Tensile stress was discovered to emerge with the ensuing increase of the lattice constant: $a(\mathrm{Ni}) = 3.53$ Å ($a_{\mathrm{tab}}(\mathrm{Ni}) = 3.524$ Å). When fused, the source powder forms the compound FeCr, whose mass fraction may range up

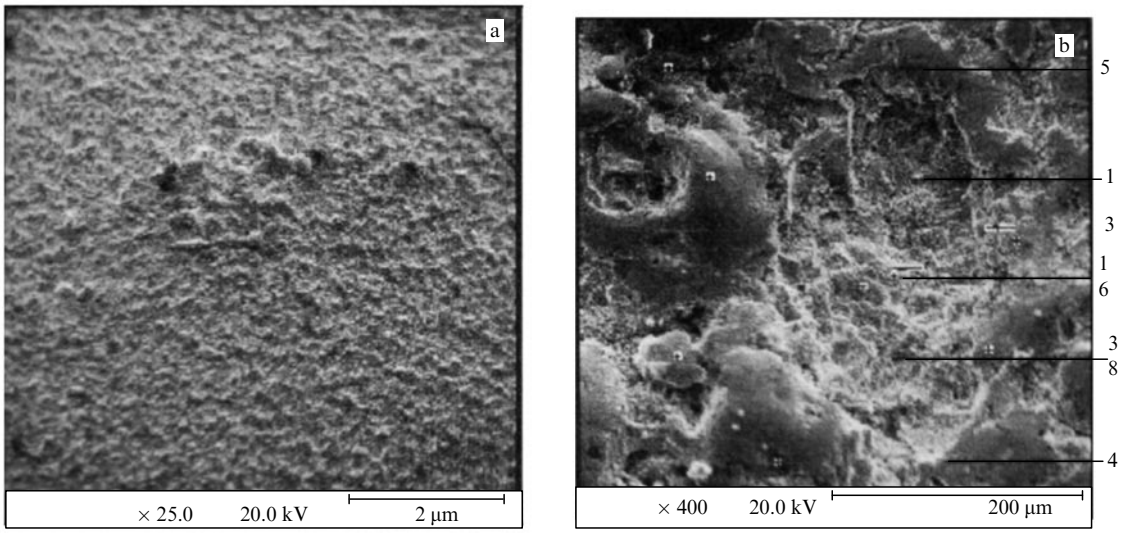

Figure 21. Microphotographs (a, b) of a part of the surface of a powder (PGAN-33) coating produced by high-speed pulsed plasma spraying wherein elemental analysis was performed, with indications of the spots of local microanalysis.

to 15%. Furthermore, an intermetallide compound Fe_7Mo_6 and possibly FeMo are formed in the coating [an evident rise of the background in X-ray diffraction patterns in the $2\theta = (42 - 50)^\circ$ region]. They account, respectively, for 12% and 4% of the total surface coating composition.

It is worth noting that after HEB processing of the PG-10N-01 coating surface, a wavy microrelief forms on it, with shallow dents observed in some places. An investigation of the surface relief of these dents showed that they are clusters of small inclusions, which comprise significant fractions of S, Al, and Ta according to the data of elemental analysis. But the main element is iron. Nonuniformly distributed dark regions were discovered on the surface, in which the highest density of the main component — iron — amounts to about 94% (this follows from an analysis of the spectra recorded for one such spot on the coating). The integral characteristic of the elemental surface composition after electron-induced fusion testifies to a nearly six-fold increase in iron density relative to the iron fraction in the source powder material. Most likely, during e-beam surface fusion, complete melting of the powder coating occurs with a partial fusion of the substrate surface and local mixing of the components of the substrate and the coating. In addition, the coating comprises about 15% Cr and 40.5% Ni.

The e-beam fusion of the coating surface was found to have a strong effect on its resultant composition. As revealed by an analysis of X-ray diffraction patterns, the source PG-10N-01 powder contains 72% Ni, 20% FeCr, and 8% CrB. The HEB-induced surface fusion has the effect that the main constituents of the coating are Ni and Fe. They account, respectively, for about 65% and 6% of the total phase composition of the surface. The Ni lattice is strongly extended, $a\,(\mathrm{Ni}) = 3.55$ Å, and the lattice constant of α-Fe is equal to 2.86 Å. Owing to the coating modification, oxide compounds Ni_2O_3 (9%), NiO (4%), and Fe_2O_3 (9%) simultaneously form on the surface. The coating surface also comprises about 6.5% Cr.

Based on an analysis of the photographs of the PG-10N-01 coating surface obtained after its HEB processing in the hard regime and after pulsed plasma processing, one can draw the conclusion that the plasma-detonation coating is accompanied by the formation of a granular structure. HEB surface processing has the effect that these grains are fused together to make the surface more uniform. We emphasize that the coating exhibits a small number of small pores (round and oval regions). After pulsed-plasma modification, they turn out to be greater in dimensions and number than after HEB surface modification. But the formation of a granular structure is more pronounced in such coatings. Investigations of the phase composition performed for the HEB-processed coatings in the hard regime yielded the following results. The coating is comprised of 50% Ni [$a\,(\mathrm{Ni}) = 3.54$ Å] and 11% Cr [$a\,(\mathrm{Cr}) = 2.88$ Å] [94].

Increasing the HEB power density in the irradiation of coatings was responsible for the growth of the surface density of the main component of the substrate matrix — iron — and for the formation of intermetallide compounds of constituent elements of the powder. An X-ray diffraction pattern clearly shows the peaks corresponding to the CrB and FeCr compounds, whose respective mass fractions in a coating approximately 1 μm thick are equal to 13% and 26%.

The greatest increase in microhardness was observed for samples exposed to the electron beam at the highest power density. Upon fusion, the surface microhardness increased 4.5-fold relative to the initial substrate material. A gain in microhardness is clearly observed at a depth greater than 300 μm. At the same time, when the coating was irradiated by the electron beam with a partial fusion of the substrate, the hardness increased by a factor slightly greater than three and, accordingly, the maximum depth of the hardened layer was only about 100 μm, i.e., was approximately equal to the thickness of the powder coating itself. The microhardness of the coating not processed by the electron beam (immediately after deposition by a high-speed pulsed plasma jet) is significantly lower than after the thermal surface annealing by the electron beam. It was determined that the range of thermal action of the plasma jet amounts to about 200 μm and the range of thermal action of the electron beam in the hard fusion mode to 500 μm.

The analysis of the wear as a function of the number of rotations and their wear time shows that the efficiency of the plasma detonation coating is equal to approximately 2, and of the e-beam technology to 9 for the soft regime and to 90 for the hard regime. This may be attributed to the fact that the HEB processing in the soft regime reduces the porosity of the Ni-alloy coating surface, and upon HEB processing in the hard regime, there occurs fusion of the coating and mixing of the surface coating layer with the base. Furthermore, the increase in wear resistance of sample surfaces upon plasma detonation processing and HEB processing may be attributed to changes in the structural phase state of the surface.

It is pertinent to note that the minimal deterioration corresponds to the e-beam processing regime whereby the coating is fused and the substrate surface is fused to a depth approximately equal to the coating thickness.

Referring to Table 8, the best corrosion test results were obtained for samples with a coating modified by the electron beam (the lowest corrosion potential E, corrosion currents i_{cor}, and passivation currents i_{pas}). This corrosion resistance is attributable to the fact that the surface was fused, the grains were made finer, porosity was lowered, and, most important, redistribution of elements near the coating surface occurs.

Figure 22 shows the image of a coating surface near the 'triple point'. One can see that roughness has decreased throughout the irradiated part of the sample, but there are regions with a very large roughness produced due to the fusion. There are regions with incompletely dissolved powder particles (most likely, these are regions of refractory elements and their carbides).

Therefore, investigations into the elemental composition of powder coatings suggest that Ni is the main surface component of the coatings subjected to e-beam processing. The e-beam irradiation with the consequential component mixing entails the emergence of substrate constituents in the nickel matrix of the coating. An interplay has been established between the phase composition, chemical composition,

Table 8. Corrosion test data for nickel-alloy-coated samples in a sulfuric acid solution with the molar density 0.5M.

Sample	E, mV	i_{cor}, mA	i_{pas}, mA	E_{pas}, mV
Unprocessed substrate	– 685	5.7	2.52	1352
Powder coating	– 330	0.78	1.1	1035
Powder coating with subsequent e-beam processing	– 278	0.59	0.82	984

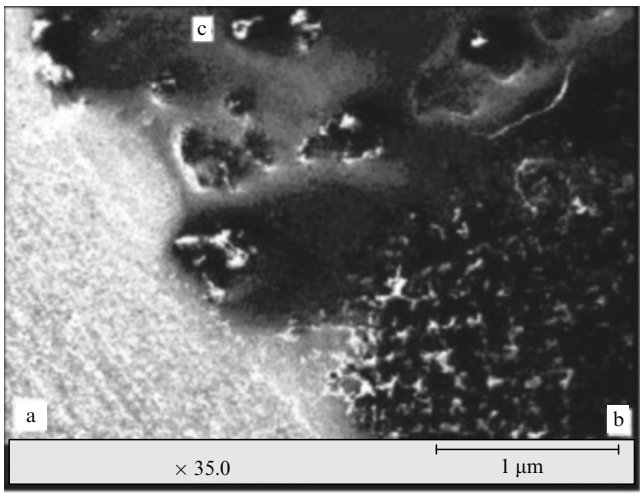

Figure 22. SEM image obtained near the 'triple point': (a) oblique section, (b) surface after coating deposition, (c) coating surface fused with the electron beam

and morphology of coating surfaces processed with an e-beam and the following mechanical characteristics: microhardness, friction wear, and resistance to corrosion in a solution of sulfuric acid and an acid environment.

The reasons for the change in operational characteristics are as follows: a decrease in grain size (from dozens of micrometers to a few micrometers or hundreds of nanometers), the healing of pores, a strengthening of coating–substrate adhesion, and the supposed reduction of roughness size due to e-beam-induced fusion.

6. Pulsed plasma interaction with a metal surface

It is well known that the action of concentrated energy sources involves a rapid (in $10^{-3}-10^{-6}$ s) heating of the surface metal layer with its subsequent intense cooling by heat removal both into the metal volume and into the surrounding medium. The high rates of heating and cooling of the surface metal layer (10^4-10^8 K s^{-1}) favor the formation of a disperse crystal structure and a high dislocation density, as well as changes in carbon and nitrogen densities [95, 96].

The thermal action by concentrated energy sources is combined with alloying procedures. The surfaces of articles are alloyed by fusing previously deposited coatings [97] or by introducing different gaseous doping impurities into the working medium (plasma): nitrogen, hydrocarbon gases, and cyanides [54]. Research shows that pulsed action on the surface of an article is most efficient. This is due to the higher rates of heating and cooling, elastoplastic deformation of the surface, and the consequential intensification of virtually all known diffusion mechanisms [97].

The growth of diffusion coefficients for a rapid elastoplastic deformation is attributable to the increase in the average dislocation density, which exceeds the equilibrium one. According to the investigations in Refs [84–86], in the rapid plastic deformation of crystalline bodies, the rate of atomic migration in them exceeds the rate of diffusion transfer of elements in a liquid metal. At the point of applied shock produced by a hard blow on the surface of a sample (the deformation time $\tau = 4 \times 10^{-3}$ s, the extent of deformation 10%, the temperature in the contact zone 800 °C), the diffusion coefficient ($D = 8.3 \times 10^{-3}$ cm^2 s^{-1}) is two orders of magnitude higher than in the liquid metal [95]. In a similar manner, mass transfer is enhanced by rapid deformation in a pulsed magnetic field.

The investigations in Refs [84–86] showed that the mass transfer coefficient increases in any pulsed processing of the surface of an article and depends only slightly on the grain size. With an increase in the number of pulses, the mass transfer coefficient decreases monotonically. Most interestingly, the simultaneous action of different kinds of pulsed processing on the surface of an article substantially enhances mass transfer and this enhancement is inherently synergetic.

Transient detonation regimes of combustion of gaseous mixtures were employed with the goal of efficiently generating high-power plasma jets [95].

When a pulsed plasma jet is ejected from the plasmatron, it closes the electric circuit between the anode electrode and the article surface (the cathode). The passage of electric current along this jet heats the plasma due to the Joule heat release $Q = \sigma E^2$ V m^{-3}.

The energy characteristics of plasma jets at the plasmatron output depend linearly on the electric field strength and the interelectrode gap width. For the interelectrode gap width $L = 200$ mm and the electric field strength 400 kV m^{-1}, the plasma jet may have the temperature 15,000 K and the velocity 5 km s^{-1}.

The plasma jet characteristics were experimentally determined on an industrial plasmatron with the interelectrode gap width 200 mm. Spectral analysis of the plasma jet yielded the value of temperature averaged over the plasma jet lifetime. The plasma temperature was determined from the relative intensity of iron lines. The time-integrated plasma emission spectra show that the plasma temperature at the plasmatron output is equal to 15,000–20,000 K.

In high-speed photography of plasma jets, they exhibited compression shocks and periodic structures (Figs 23a and 23b). Measurements of the initial jet diameter (the diameter of the generator nozzle) and the distance to the first compression shock permit calculating the jet velocity. One can see from the photograph that the first shock practically consists of two. This is due to the nonuniformity of the plasma jet, which consists of jets with different velocities. We estimate the jet velocity V by the formula

$$L_w = 1.3 d_a \sqrt{\mathrm{M}^2 - 1}\,, \tag{15}$$

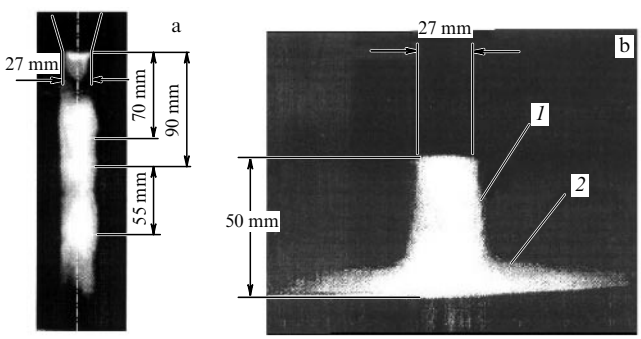

Figure 23. (a) A plasma jet freely emanating from the plasmatron nozzle, (b) high-speed photography of the interaction of the pulsed plasma jet with a barrier (substrate-target): 1 — plasma jet, 2 — shock-compressed layer

which we rewrite as

$$V = a_0 \sqrt{\left(\frac{L_w}{1.3 d_a}\right)^2 + 1}\,, \tag{16}$$

where $d_a = 0.027$ m is the diameter of the plasmatron nozzle, $M = V/a_0$ is the Mach number, $L_{w_1} = 70$ mm, and $L_{w_2} = 90$ mm is the wavelength of the periodic structure whose image was recorded by the high-speed photography. The sound velocity a_0 is determined by the formula

$$a_0 = \sqrt{\gamma R T}\,, \tag{17}$$

where, in our case, $\gamma = 1.3$ is the adiabatic exponent, $R = 300$ J (kg K)$^{-1}$ is the gas constant, and $T = 15000$ K is the jet temperature.

We substitute expression (16) into formula (17) to obtain $V_1 = 5.4$ km s^{-1} and $V_2 = 6.7$ km s^{-1}, which is consistent with theoretical data.

The plasma jet structure is typical of a supersonic jet flow in the underexpansion mode and corresponds to the explosive nature of plasmatron operation, whereby the pressure in the chamber may significantly exceed the ambient pressure. The plasma jet – barrier interaction picture is characterized by the existence of the plasma jet *1* and shock-compressed layer (SCL) *2* (see Fig. 23), which is quite typical [93].

Upon breakdown of the SCL, the electric current flows through the plasma jet from the central electrode in the plasmatron to the surface of the article being processed. The electric current density in the plasma jet is $J = (1-7) \times 10^3$ A cm^{-2} and the temperature $T = 15{,}000$ – 30,000 K. The thermal flux into the article depends on the electric current density and varies in the range $q = (0.1-5) \times 10^6$ W cm^{-2}. The thermal fluxes were estimated on the basis of a theoretical analysis of the transient heat conduction equation from the thickness of the hardened layer of martensite-class steels [95].

The duration of plasma-pulse action and its energy characteristics were controlled by varying the capacitance C, the voltage U_{ch} across the capacitor bank plates, the inductance L in the discharge circuit, the distance to the article surface H, and the dimension of the active plasma-jet – article interaction spot.

Experiments were staged to measure the temporal variation of electric current across the interelectrode gap, as well as the current between the central electrode and the surface of the article. The experiments were carried out with the use of Rogowski loops by the well-known method [86] for the following characteristics: $C = 1000$ μF, $U_{ch} = 3500$ V, $H = 70$ mm, $L = 3 \times 10^{-5}$ H. An analysis of the temporal current distribution suggests that the electric resistance of the SCL, which forms when the plasma jet impinges on the article surface, is much higher than the resistance of the discharge gap between the coaxial electrodes. The measurements showed that the SCL breakdown occurs in only 1.2 ms. During this period, the capacitors manage to become recharged and the expendable electrode is the cathode for 0.2 ms and then the anode again for 0.4 – 0.6 ms.

The experiments revealed that the article surface initially experiences elastodeformation interaction with the shock wave and the pulsed plasma jet; then, in the SCL breakdown, the surface experiences the action of electric current. The amplitude of the current is 5 kA. There results a pulsed magnetic field up to 2000 Oe. Subsequently, for 3 – 5 ms, combustion and electrode erosion products flow onto the surface.

A hardened alloyed layer forms as a result of pulsed-plasma processing of articles made of an iron-based alloy. The occurrence of apparent defects in the layer depends on the plasma composition and the number of processing pulses. For instance, oxide inclusions are seen in the layer after processing by a plasma with increased oxygen content ($\alpha > 1$). No oxides were discovered after precisely the same processing but with $\alpha < 0.8$ ($\alpha = \chi/\chi^0$ is the excess oxidizer coefficient, $\chi^0 = \nu(O_2)/\nu(C_nH_m)$ is the molar stoichiometric ratio, and χ is the actual component ratio). For an oxygen-propane mixture, $\chi^0 = 5$. The hardened layer has a greater thickness and homogeneity after multiple (5 pulses) pulsed-plasma processing.

The greatest hardness of the hardened layer on U8 steel samples, which had preliminarily been subjected to heat strengthening and high-temperature tempering, was achieved with the use of tungsten and molybdenum electrodes. The processing was effected without surface fusion, and the specific jet power was equal to 10^6 W cm^{-2}. Microhardness was measured on transverse metallographic sections using a PMT-3 hardness meter and a diamond Knoop pyramidion. The pyramidion load was $P = 100$ G.

The results of investigations of U8A steel samples performed with a Neopot-2 microscope and a T-20 scanning electron microscope show that the near-surface layer is characterized by the presence of numerous white globules up to 3.5 μm in size. X-ray diffraction patterns from the surface of U8 and constructional steel samples processed under the same regimes exhibit the same phase composition. The Auger spectra of a processed steel surface contain high-intensity carbon, titanium, and nitrogen peaks, the intensities of iron peaks are appreciably lower, and the dark spots on the surface consist almost entirely of carbon.

X-ray phase analysis of the surface layers of carbon – steel samples strengthened by a pulsed plasma jet reveals the broadening of α-Fe lines and the emergence of the lines of residual Fe austenite. Increasing the number of pulses is accompanied by further broadening of the α-Fe lines for a reduction of their intensity, as well as by a growth in the relative intensity of γ-Fe lines. Judging by the residual austenite – ferrite line intensity ratio, the amount of austenite for the same processing regime is highest when a tungsten electrode is used. X-ray spectrum investigations showed that the material of the expendable electrode penetrates the hardened layer of the article. For instance, when the expendable electrode was made of titanium, it was discovered in the hardened layer at depths up to 20 μm [95].

The magnitude of mass transfer of light elements was determined by Auger spectroscopy techniques. The samples were made of 9KhS tool steel (0.93% C, 1.4% Si, 1.1% Cr, 0.35% Ni, 0.4% Mn, 0.03% S, 0.03% P). The elemental density distribution according to the depth of the layer was investigated on the LAS-2000 facility using oblique sections tilted by 8° to the surface. The measurement data were averaged by a fifth-degree polynomial by finding the minimum of the merit function (the root-mean-square deviation) in the Mathcad 7 Professional environment on a computer.

Experiments showed that article surface irradiation by thirty plasma pulses ($\tau_p = 0.6$ ms) has the effect that the nitrogen density at the depth 20 μm ranges up to 3.2 at. %. A similar elemental density distribution is attainable under

thermal diffusion assuming the mass transfer coefficient of the order of $D = 10^{-4} - 10^{-5}$ cm^2 s^{-1}.

By way of Auger spectroscopic investigations, it was determined that the pulsed plasma processing of cast iron rollers produces a surface layer containing molybdenum, tungsten, chromium, titanium, carbon, iron, oxygen, and other dopants, depending on the composition of the electrode employed. At depths under the strengthened layer, there are also molybdenum and carbon, whose peaks prevail over the iron lines. The fused layer of cast iron is acicular crystalline in structure and contains globules of the electrode material. The layer microhardness at depths of 80 – 100 μm is equal to 10 – 14 GPa.

The pulsed-plasma strengthening is achieved due to ultrafast cooling of the article surface alloyed in the molten state. The nonabrupt cluster boundaries and the 'freezing' owing to supercooling lead to the formation of metastable structures with extremely strong fragmentation of structural elements. This is demonstrated by transmission electron microscopy data, as well as by the form of fracture.

The additional structural fragmentation arising from plasma processing is confirmed by the occurrence of a nearly continuous thin circle in the electron-diffraction pattern corresponding to the (110) reflexes of α-Fe [95].

Upon solid-phase article processing by the pulsed plasma, X-ray phase analysis revealed high-intensity austenite lines in the modified layer, which become stronger with processing intensification. The conclusion was reached on the strength of literature data that this is due to the development of crystallographic texture in the case of phase recrystallization under cooling in the presence of a strong temperature gradient. It is well known that the ⟨001⟩ direction in crystalline materials with a cubic lattice is, under these conditions, oriented mainly along the temperature gradient, which manifests itself in a rise in the relative intensity of the (200) line.

An investigation of the broadening of X-ray diffraction lines showed that the after-plasma-processing broadening of both α-Fe lines and γ-Fe lines may be considered to be proportional to tan Q, which indicates that inhomogeneous elastic lattice distortions make the dominant contribution to the broadening [95]. These distortions may arise from elastic deformations due to dislocations and/or the coherent coupling of particles of different phases, as well as from the nonuniform distribution of dopants, in particular titanium, nitrogen, and carbon.

7. Conclusion

We have considered one avenue in technology — the use of thermal plasmas for producing new materials and nanodimensional powders, depositing combined and protective coatings, and modifying the surfaces of materials by exposing them to pulsed plasma jets. We have shown that the findings of an investigation into this technological sphere may be used to advantage in many branches of industry. At present, the employment of pulsed high-speed jets offers promise as a tool for obtaining new composite, highly doped materials on the surfaces of articles made of constructional materials.

The thermal plasma processing of metal surfaces is under development and will soon enjoy wide use for the compaction of powdered materials, coatings, plasma-chemical vapor-phase coating deposition, and the synthesis of fine powders with nanometer-sized grains. The industrial development of these technologies is largely dependent on the progress and application of the methods for efficient inspection of the technology, and the resultant coatings and materials.

Acknowledgements. This work was supported by the Ukrainian Science and Technology Center under Project No 3078; the NATO Linkage Collaborative Grant No. 957618; the Projects of the National Academy of Sciences of Ukraine "Nanosystems, nanomaterials, and nanotechnologies (new physical principles of producing nanofilms, nanotechnologies, and coatings with the aid of electron, ion, and plasma flows)"; and the Project No. 6/33 "Development of physicometallurgic foundations of complex surface doping of iron-based alloys."

For assistance in the preparation of this investigation, the authors are grateful to O V Kolisnichenko, M L Zhadkevich, and A A Bondarev of the Institute for Electric Welding, National Academy of Sciences of Ukraine; to O P Kul'ment'eva, V S Kshnyakin, Yu A Kravchenko, M V Il'yashenko, A G Boiko, V V Ponaryadov, and Sh M Ruzimov of the Sumy Institute for Surface Modification; to D L Alontseva and M K Kalyshkanov of East-Kazakhstan State Technical University; to M A Vasil'ev, V F Mazenko, and O M Ivasishin of the Metallophysics Institute, National Academy of Sciences of Ukraine; and to P Misaelidis (Thessaloniki, Greece), S Kuroda (Tsukuba, Ibaraki, Japan), J Han (Suwon, Korea), and W Zhao (Beijing, China).

References

1. Smith R W, Novak R *Powder Metall. Int.* **23** 147 (1991)
2. Smith R W, Novak R *Powder Metall. Int.* **23** 231 (1991)
3. Pober R, Abbott R *Am. Ceram. Soc. Bull.* **73** (2) 45 (1994)
4. Boulos M *J. Thermal Spray Technol.* **1** 33 (1992)
5. Steffens H-D, Babiak Z, Wewel M *IEEE Trans. Plasma Sci.* **PS-18** 974 (1989)
6. Thorpe M L *Adv. Mater. Process.* **134** (4) 69 (1988)
7. Marantz D R, Marantz D R, in *Thermal Spray Research and Applications: Proc. of the 3rd National Thermal Spray Conf., Long Beach, Calif., USA, 20 – 25 May 1990* (Ed. T F Bernecki) (Materials Park, OH: ASM Intern., 1991) p. 113
8. Sampson E, Nieder L, in *Thermal Spray Coatings: Research, Design, and Applications: Proc. of the 5th National Thermal Spray Conf., June 7 – 11, 1993, Anaheim, Calif., USA* (Eds C C Berndt, T F Bernecki) (Materials Park, OH: ASM Intern., 1993) p. 251
9. Sampson E, in *Thermal Spray Coatings: Research, Design, and Applications: Proc. of the 5th National Thermal Spray Conf., June 7 – 11, 1993, Anaheim, Calif., USA* (Eds C C Berndt, T F Bernecki) (Materials Park, OH: ASM Intern., 1993) p. 257
10. Wang X et al., in *Advances in Thermal Spray Science and Technology: Proc. of the 8th National Thermal Spray Conf., 11 – 15 September, 1995, Houston, Texas, USA* (Eds C C Berndt, S Sampath) (Materials Park, OH: ASM Intern., 1995) p. 31
11. Heberlein J, Pfender E *Mater. Sci. Forum* **140/142** 477 (1993)
12. Ohtake N, Yoshikawa M *J. Electrochem. Soc.* **137** 717 (1990)
13. Ohtake N et al., in *Applications of Diamond Films and Related Materials: Proc. of the 1st Intern. Conf., ADC'91, Auburn, Alabama, USA, August 17 – 22, 1991* (Eds Y Tzeng et al.) (Amsterdam: Elsevier, 1991) p. 431
14. Pfender E et al. *Diamond Relat. Mater.* **1** 127 (1992)
15. Yoshida T et al. *J. Appl. Phys.* **54** 640 (1983)
16. Kumar A, Roy R *J. Mater. Res.* **3** 1373 (1989)
17. Kong P, Pfender E, in *Ceramic Powders Processing Science: Proc. of the 2nd Intern. Conf., Berchtesgaden, Bavaria, FRG, October 12 – 14, 1988* (Eds H Hausner, G L Messing, S Mirano) (Köln: Deutsche Keramische Gesellschaft, 1989)
18. Kong P, Pfender E, in *Combustion and Plasma Synthesis of High-Temperature Materials* (Eds Z A Munir, J B Holt) (New York: VCH, 1990) p. 420

19. Kong P et al., in *Better Ceramics Through Chemistry IV* (Mater. Res. Soc. Symp. Proc., Vol. 180, Eds B J J Zelinski et al.) (Pittsburgh, Pa.: Materials Res. Soc., 1990) p. 849
20. Or T et al., in *Plasma Processing and Synthesis of Materials III* (Mater. Res. Soc. Symp. Proc., Vol. 190, Eds D Apelian, J Szekely) (Pittsburgh, Pa.: Materials Res. Soc., 1991) p. 83
21. Zhu H, Lau Y, Pfender E, in *LOOKRF Plasma Synthesis of YBa_2Cu_{7-x} Powders Using a Liquid Injection Method* O Talk Summaries, Electronics Division, presented at the 91st Annual Meeting of the American Ceramic Society (Ed. K M Nair) (Indianapolis: American Ceramic Society, 1989) p. 173
22. Kong P, Pfender E, in *LOOKRF Plasma Synthesis of YBa_2Cu_{7-x} Powders Using a Liquid Injection Method* O Talk Summaries, Electronics Division, presented at the 91st Annual Meeting of the American Ceramic Society (Ed. K M Nair) (Indianapolis: American Ceramic Society, 1989) p. 378
23. Terashima K, Yoshida T, Akashi K *Jpn. Symp. Plasma Chem.* **8** (3) 157 (1988)
24. Ono T et al. *Plasma Chem. Plasma Process.* **7** (2) 201 (1987)
25. Zu H, Lau Y, Pfender E, in *ISPC-9: Intern. Symp. on Plasma Chemistry, Pughochiuso, Italy, 1989* (Ed. R D Agostino) (Bari: Univ. of Bari, 1989) p. 1497
26. Kong P, Pfender E, in *Non-Oxide Ceramic Engineering* (Eds A W Weimer, W Rafaniello) (London: Chapman and Hall) (in press)
27. Siegel R W *Mater. Sci. Eng. A* **168** 189 (1993)
28. Grishick S L, Chiu C-P *Plasma Chem. Plasma Process.* **9** 355 (1989)
29. Rao N et al. *Plasma Chem. Plasma Process.* **15** 581 (1995)
30. Boulos M, Pfender E *MRS Bull.* **21** (8) 65 (1996)
31. Tyurin Y N, Pogrebnjak A D *Surf. Coat. Technol.* **111** 269 (1999)
32. Pogrebnyak A D et al. *Pis'ma Zh. Tekh. Fiz.* **26** (21) 53 (2000) [*Tech. Phys. Lett.* **26** 960 (2000)]
33. Pogrebnyak A D et al. *Zh. Tekh. Fiz.* **71** (7) 111 (2001) [*Tech. Phys.* **46** 897 (2001)]
34. Lebedev A D, Uryukov B A *Impul'snye Uskoriteli Plazmy Vysokogo Davleniya* (Pulsed High-Pressure Plasma Accelerators) (Novosibirsk: Inst. Teplofiz. SO AN SSSR, 1990) p. 280
35. Uglum J R et al. *ASM Thermal Spray Soc.* **7** 373 (1997)
36. Bhagat R B et al. *ASM Thermal Spray Soc.* **7** 361 (1997)
37. Pogrebnjak A D et al. *Vacuum* **62** 21 (2001)
38. Pogrebnjak A D, Kul'ment'eva O P, Tyurin Yu N, in *New Electrical and Electronic Technologies and Their Industrial Implementation, NEET-2001: II Intern. Symp., 14 – 17 February 2001, Lublin, Poland* (Ed. K Dolny) (Lublin: Lublin Univ. of Technology, 2001) p. 119
39. Tyurin Yu N "Sposob Detonatsionnogo Naneseniya" ("Method of Detonation Coating"), USSR Inventor's Certificate No. 1045491 (1983)
40. Kharlamov Yu A "Detonatsionno-Gazovye Ustanovki dlya Naneseniya Pokrytiĭ" ("Gas-Detonation Facilities for Coating Deposition"), Deposit in UkrNIINTI of 25.08.88, No. 2101-UK88 (Voroshilovgrad, 1988) p. 22
41. Pogrebnyak A D et al. *Metallofiz. Noveĭshie Tekhnol.* (2005) (in press)
42. Pogrebnyak A D et al. *Fiz.-Khim. Osnovy Materialoved.* (1) 35 (2005)
43. Zhadkevich M L et al. *Probl. Metallurgii, Svarki, Materialoved.* (Tbilisi) (3(5)) 24 (2004)
44. Pogrebnyak A D et al. *Pis'ma Zh. Tekh. Fiz.* (2005) (in press)
45. Pogrebnyak A D et al. *Fiz. Inzheneriya Poverkh.* (Khar'kov) **1** (34) 52 (2003)
46. Heath G R, Dumola R J, in *Thermal Spray: Meeting the Challenges of the 21st Century: Proc. of the 15th Intern. Thermal Spray Conf., 25 – 29 May 1998, Nice, France* (Ed. C Coddet) (Materials Rark, OH: ASM Intern., 1998) p. 1495
47. Miyamoto M, Sakutatu T, Tago M, in *Thermal Spray: Meeting the Challenges of the 21st Century: Proc. of the 15th Intern. Thermal Spray Conf., 25 – 29 May 1998, Nice, France* (Ed. C Coddet) (Materials Rark, OH: ASM Intern., 1998) p. 1501
48. Thorpe M L, Richter H J, in *Thermal Spray: Intern. Advances in Coatings Technology: Proc. of the Intern. Thermal Spray Conf., 28 May – 5 June 1992, Orlando, Fl., USA* (Materials Park, OH: ASM Inter., 1992) p. 137
49. Tyurin Yu N *Avtomaticheskaya Svarka* (5) 13 (1999)
50. Lebedev A D, Uryukov B A *Uskoriteli Plazmy Vysokogo Davleniya* (High-Pressure Plasma Accelerators) (Novosibirsk, 1995) p. 210
51. Pogrebnyak A D et al., in *Plenki i Pokrytiya — 2001: Trudy 6-ĭ Mezhdunarodnoĭ Konf., 3 – 5 Aprelya 2001 g., St. Petersburg* (Films and Coatings – 2001: Proc. of the 6th Intern. Conf., 3 – 5 April, 2001, St. Petersburg) (Ed. V S Klubnikin) (St. Petersburg: Izd. SPbGTU, 2001) p. 56
52. Tyurin Yu N et al., in *Plenki i Pokrytiya — 2001: Trudy 6-ĭ Mezhdunarodnoĭ Konf., 3 – 5 Aprelya 2001 g., St. Petersburg* (Films and Coatings – 2001: Proc. of the 6th Intern. Conf., 3 – 5 April, 2001, St. Petersburg) (Ed. V S Klubnikin) (St. Petersburg: Izd. SPbGTU, 2001) p. 71
53. Pogrebnyak A D, Tyurin Yu N, Kobzev A P *Pis'ma Zh. Tekh. Fiz.* **27** (15) 1 (2001) [*Tech. Phys. Lett.* **27** 619 (2001)]
54. Pogrebnyak A D et al. *Fiz.-Khim. Osnovy Materialoved.* (4) 47 (2001)
55. Belikova A F et al. *Fiz.-Khim. Osnovy Materialoved.* (9) 100 (1989)
56. Pogrebnyak A D et al., in *New Electrical and Electronic Technologies and Their Industrial Implementation, NEET-2001: II Intern. Symp., 14 – 17 February 2001, Lublin, Poland* (Ed. K Dolny) (Lublin: Lublin Univ. of Technology, 2001) p. 51
57. Pogrebnyak A D et al. *Pis'ma Zh. Tekh. Fiz.* **30** (4) 78 (2004) [*Tech. Phys. Lett.* **30** 164 (2004)]
58. Pogrebnyak A D et al., in *Plenki i Pokrytiya — 2001: Trudy 6-ĭ Mezhdunarodnoĭ Konf., 3 – 5 Aprelya 2001 g., St. Petersburg* (Films and Coatings — 2001: Proc. of the 6th Intern. Conf., 3 – 5 April, 2001, St. Petersburg) (Ed. V S Klubnikin) (St. Petersburg: Izd. SPbGTU, 2001) p. 324
59. Pogrebnyak A D et al., in *Plenki i Pokrytiya — 2001: Trudy 6-ĭ Mezhdunarodnoĭ Konf., 3 – 5 Aprelya 2001 g., St. Petersburg* (Films and Coatings – 2001: Proc. of the 6th Intern. Conf., 3 – 5 April, 2001, St. Petersburg) (Ed. V S Klubnikin) (St. Petersburg: Izd. SPbGTU, 2001) p. 82
60. Pogrebnyak A D et al. *Fiz. Met. Metalloved.* (5) 45 (2004) [*Phys. Met. Metallogr.* **97** 470 (2004)]
61. Pogrebnjak A D et al., in *6th Intern. Symp. Sputtering & Plasma Processes, ISSP 2001, Kanazawa, Japan, June 13 – 15 2001* (Kanazawa, 2001) p. 92
62. Yuschenko K A, Borisov Y S, Tyurin Yu N "Method and device for plasma-detonation working of metal articles", European Patent № 0531527 Al. (1991)
63. Voss A et al. *Thin Solid Films* **220** 116 (1992)
64. Gavrilenko T P, Nikolaev Y A, Ulianitsky V Y, in *Thermal Spray: Meeting the Challenges of the 21st Century: Proc. of the 15th Intern. Thermal Spray Conf., 25 – 29 May 1998, Nice, France* (Ed. C Coddet) (Materials Rark, OH: ASM Intern., 1998) p. 1485
65. Lugscheider E, Oberlander B C *Sci. Rev.* **88** (5) 283 (1991)
66. *Modelling of Laser Hard-Facing of Steels with Carbide Powder Injection* (BRITE/EURAM Programme) (Luxemb.: OOPEC, 1990) p. 337
67. Pogrebnyak A D et al. *Pis'ma Zh. Tekh. Fiz.* **29** (24) 35 (2003) [*Tech. Phys. Lett.* **29** 1028 (2003)]
68. Pogrebnjak A D et al., in *New Electrical and Electronic Technologies and Their Industrial Implementation: III Intern. Symp., Zakopane, Poland, May 13 – 16, 2003* (Lublin: Lublin Univ. of Technology, 2003) p. 154
69. Pogrebnjak A D et al., in *New Electrical and Electronic Technologies and Their Industrial Implementation: III Intern. Symp., Zakopane, Poland, May 13 – 16, 2003* (Lublin: Lublin Univ. of Technology, 2003) p. 157
70. Rej D J et al. *Nucl. Instrum. Meth. B* **127/128** 987 (1997)
71. Pogrebnyak A D et al. *Fiz.-Khim. Osnovy Materialoved.* (2005) (in press)
72. Klimenov V A et al. *Fiz.-Khim. Osnovy Materialoved.* (6) 68 (1997)
73. Pogrebnyak A D et al. *Metallofiz. Noveishie Tekhnol.* **25** 1329 (2003)
74. Pogrebnjak A D, Ruzimov Sh M *Phys. Lett. A* **120** 259 (1987)
75. Pogrebnjak A D et al. *Phys. Lett. A* **123** 410 (1987)
76. Nakagawa Y et al. *Jpn. J. Appl. Phys.* **27** L719 (1988)
77. Nakagawa Y et al. *Nucl. Instrum. Meth. B* **39** 603 (1989)
78. Ivanov Yu F, Lykov S V, Rotshtein V P *Fiz.-Khim. Osnovy Materialoved.* (5) 62 (1993)

79. Yatsui K et al., in *Proc. of the 10th Intern. Conf. "High Power Particle Beams", San-Diego, USA, June 16 – 25, 1994* (San Diego, 1994) p. 27
80. Davis H A et al. *MRS Bull.* **21** 58 (1996)
81. Davis H A et al. *Mater. Chem. Phys.* **54** 213 (1998)
82. Proskurovsky D I et. al. *Vac. Sci. Technol. A* **16** 2480 (1998)
83. Misaelides P et al. *Surf. Coat. Technol.* **180 – 181** 290 (2004)
84. Tyurin Y N, Pogrebnyak A D *Surf. Coat. Technol.* **142 – 144** 293 (2001)
85. Gertsriken D S, Mazanko V F, Fal'chenko V M *Impul'snaya Obrabotka i Massoperenos v Metallakh pri Nizkikh Temperaturakh* (Pulsed Processing and Mass Transfer in Metals at Low Temperatures) (Kiev: Naukova Dumka, 1991)
86. Tyurin Yu N, Kolisnichenko O V, Tsygankov N G *Avtomaticheskaya Svarka* (1) 38 (2001)
87. Misaelides P et. al. *Nucl. Instrum. Meth. B* (2005) (in press)
88. Pogrebnjak A D et al., in *Proc. of the 7th Intern. Conf. on Modification of Materials with Particle Beams and Plasma Flows, 25 – 27 July 2004, Tomsk, Russia* (Tomsk, 2004) p. 417
89. Itin V I et al., in *Proc. of the 3rd Intern. Conf. "Energy Pulse and Particle Beam Modification of Materials", September 4 – 8 1989, Dresden, GDR* (Phys. Res., Vol. 13, Eds K Hohmuth, E Richter) (Berlin: Akademie Verlag, 1990); *Surf. Coat. Technol.* **142 – 144** 293 (2001)
90. Valyaev A N, Kishimoto N, Pogrebnyak A D *Modifikatsiya Svoistv Materialov i Sintez Tonkikh Plenok pri Obluchenii Intensivnymi Elektronnymi i Ionnymi Puchkami* (Modification of Material Properties and Thin-Film Synthesis by High-Intensity Electron and Ion Beam Irradiation) (Ust'-Kamenogorsk: Vostochno-Kazakhstanskii Tekhnicheskii Univ., 2000) p. 345
91. Boiko V I et al. *Fiz.-Khim. Osnovy Materialoved.* (1) 29 (1992)
92. Boiko V I et al. *Fiz.-Khim. Osnovy Materialoved.* (5) 28 (1993)
93. Zhadkevich M L et al. *Probl. Metallurgii, Svarki, Materialoved.* (Tbilisi) (1(3)) 26 (2004)
94. Zhetbaev A K et al. *Fazovye Preobrazovaniya v Implantatsionnykh Sistemakh Metall – Metalloid* (Phase Transformations in Metal–Metalloid Implantation Systems) (Alma-Aty: Gylym, 1995) p. 182
95. Pogrebnyak A D, Tyurin Yu N *Usp. Fiz. Met.* **4** 1 (2003)
96. Prokhorov A M, in *Nauchnye Osnovy Progressivnoi Tekhnologii* (Scientific Foundations of Advanced Technology) (Ed. V N Lymzin) (Moscow: Mashinostroenie, 1982) p. 164
97. Boĭko V I, Valyaev A N, Pogrebnyak A D *Usp. Fiz. Nauk* **169** 1243 (1999) [*Phys. Usp.* **42** 1139 (1999)]